The Astrophysical Journal, 954:35 (18pp), 2023 September 1 https://doi.org/10.3847/1538-4357/ace595

SN 2020bio: A Double-peaked, H-poor Type IIb Supernova with Evidence of Circumstellar Interaction

C. Pellegrino[1,2], D. Hiramatsu[3,4], I. Arcavi[5,6], D. A. Howell[1,2], K. A. Bostroem[7,16], P. J. Brown[8,9], J. Burke[1,2], N. Elias-Rosa[10,11], K. Itagaki[12], H. Kaneda[13], C. McCully[1,2], M. Modjaz[14], E. Padilla Gonzalez[1,2], T. A. Pritchard[15], and N. Yesmin[14]

[1] Las Cumbres Observatory, 6740 Cortona Drive, Suite 102, Goleta, CA 93117-5575, USA; cpellegrino@lco.global
[2] Department of Physics, University of California, Santa Barbara, CA 93106-9530, USA
[3] Center for Astrophysics | Harvard & Smithsonian, 60 Garden Street, Cambridge, MA 02138-1516, USA
[4] The NSF AI Institute for Artificial Intelligence and Fundamental Interactions, MIT, Cambridge, MA 02139, USA
[5] The School of Physics and Astronomy, Tel Aviv University, Tel Aviv 6997801, Israel
[6] CIFAR Azrieli Global Scholars Program, CIFAR, Toronto, Canada
[7] Department of Astronomy, University of Washington, 3910 15th Avenue NE, Seattle, WA 98195-0002, USA
[8] Department of Physics and Astronomy, Texas A&M University, 4242 TAMU, College Station, TX 77843, USA
[9] George P. and Cynthia Woods Mitchell Institute for Fundamental Physics & Astronomy, College Station, TX 77843, USA
[10] INAF—Osservatorio Astronomico di Padova, Vicolo dell'Osservatorio 5, I-35122 Padova, Italy
[11] Institute of Space Sciences (ICE, CSIC), Campus UAB, Carrer de Can Magrans s/n, 08193 Barcelona, Spain
[12] Itagaki Astronomical Observatory, Yamagata, Yamagata 990-2492, Japan
[13] Kaneda Astronomical Observatory, Sapporo, Hokkaido 005-0862, Japan
[14] Department of Astronomy, University of Virginia, Charlottesville, VA 22904, USA
[15] Department of Physics, New York University, New York, NY 10003, USA
Received 2023 January 12; revised 2023 June 29; accepted 2023 July 2; published 2023 August 22

Abstract

We present photometric and spectroscopic observations of SN 2020bio, a double-peaked Type IIb supernova (SN) discovered within a day of explosion, primarily obtained by Las Cumbres Observatory and Swift. SN 2020bio displays a rapid and long-lasting initial decline throughout the first week of its light curve, similarly to other well-studied Type IIb SNe. This early-time emission is thought to originate from the cooling of the extended outer hydrogen-rich (H-rich) envelope of the progenitor star that is shock heated by the SN explosion. We compare SN 2020bio to a sample of other double-peaked Type IIb SNe in order to investigate its progenitor properties. Analytical model fits to the early-time emission give progenitor radius ($\approx$100–1500 $R_{\odot}$) and H-rich envelope mass ($\approx$0.01–0.5 $M_{\odot}$) estimates that are consistent with other Type IIb SNe. However, SN 2020bio displays several peculiarities, including (1) weak H spectral features indicating a greater amount of mass loss than other Type IIb progenitors; (2) an underluminous secondary light-curve peak that implies a small amount of synthesized ^{56}Ni ($M_{\rm Ni}$ $\approx$0.02 $M_{\odot}$); and (3) low-luminosity nebular [O I] and interaction-powered nebular features. These observations are more consistent with a lower-mass progenitor ($M_{\rm ZAMS} \approx$ 12 $M_{\odot}$) that was stripped of most of its H-rich envelope before exploding. This study adds to the growing diversity in the observed properties of Type IIb SNe and their progenitors.

Unified Astronomy Thesaurus concepts: Circumstellar matter (241); Core-collapse supernovae (304); Supernovae (1668)

Supporting material: machine-readable table

1. Introduction

While the majority of stars with initial masses $\gtrsim$8 $M_{\odot}$ end their lives as H-rich core-collapse supernovae (SNe; e.g., Janka 2012), some massive stars lose their outer H and even He envelopes and explode as stripped-envelope SNe (SESNe; e.g., Filippenko 1997; Gal-Yam 2017). A small but growing number of SNe have been observed with spectra that show similarities to both these classes (Smith et al. 2011). Classified as Type IIb SNe (SNe IIb), their spectra have H features at early times that gradually give way to He features, indicating that their progenitors were partially stripped of their outer envelopes before exploding (Woosley et al. 1994).

It is unclear what mechanisms are responsible for this mass loss. Common hypotheses include stellar winds, binary interaction, or late-stage stellar instabilities (see, e.g., Smith 2014, for a review). Recent studies have shown that mass loss is common during the late stages of massive star evolution, as inferred from early-time observations of core-collapse SNe (e.g., Ofek et al. 2014; Bruch et al. 2021; Strotjohann et al. 2021). A significant fraction of core-collapse SNe show signatures of pre-existing circumstellar material (CSM) in their early-time spectra, obtained days after their estimated explosion epochs. This CSM is the material shed by the progenitor star in the months to years before core collapse. As the SN shock breaks out of the expanding ejecta, the resulting X-ray and ultraviolet (UV) flash may ionize the surrounding CSM, producing narrow spectral features as the CSM cools and recombines (e.g., Fassia et al. 2001;

[16] LSST Catalyst Fellow.

Yaron et al. 2017). Interaction between the SN ejecta and CSM can also influence the early-time light-curve evolution (Morozova et al. 2018).

Some SNe IIb are observed to have double-peaked light curves, with rapidly fading luminosities during the first several days after explosion before the radioactive decay of ^{56}Ni synthesized during the explosion causes a rebrightening that lasts for several weeks. The early-time emission is thought to be the cooling of the extended envelope of the progenitor star that is heated by the SN shock (Soderberg et al. 2012). This shock-cooling emission (SCE) has only been extensively observed in a handful of cases, including SN 1993J (e.g., Richmond et al. 1994; Woosley et al. 1994), SN 2011dh (e.g., Arcavi et al. 2011; Ergon et al. 2014), SN 2013df (e.g., Morales-Garoffolo et al. 2014; Van Dyk et al. 2014), SN 2016gkg (Arcavi et al. 2017), SN 2017jgh (Armstrong et al. 2021), and ZTF18aalrxas (Fremling et al. 2019), among others. Most of these objects are nearby and have had follow-up observations scheduled hours after explosion, which proved crucial to observing the rapidly evolving SCE. These studies have found that SNe IIb are consistent with the explosions of stars with extended outer envelopes, with the duration of the SCE dependent on the extent of this envelope (Soderberg et al. 2012).

Numerical and analytical models of SCE can complement pre-explosion imaging in determining the progenitors of these objects. Several models have been successful in reproducing the observed early-time evolution across all wavelengths. Piro (2015, hereafter P15) is one of the first to present a one-zone analytical description of the cooling of an extended low-mass envelope shock-heated by the explosion of a compact massive core. Piro et al. (2021, hereafter P21) extend this to a two-zone model in order to better capture the emission from the outermost material in extended envelopes. Sapir & Waxman (2017, hereafter SW17) calibrate earlier models by Rabinak & Waxman (2011)—that depend on the precise density structure of the outer material—to numerical simulations for several days after explosion.

Comparing observed SCE to analytical and numerical models is one of the only ways of directly measuring the radii and stellar structure of core-collapse progenitors from SN observations. This has been done for a handful of SNe IIb as well as SNe of other subtypes, including stripped-envelope Type Ib SNe (e.g., Modjaz et al. 2009; Yao et al. 2020), short-plateau Type II SNe (Hiramatsu et al. 2021), and exotic Ca-rich transients (e.g., Jacobson-Galán et al. 2020, 2022). Analytical and numerical modeling of double-peaked SNe IIb generally yield large radii progenitors ($\approx$100–500 $R_\odot$) with low-mass ($\approx 10^{-2}$–10^{-1} $M_\odot$) extended envelopes (Piro et al. 2021, and references therein). These properties are usually in agreement with those of SNe IIb progenitors from pre-explosion Hubble Space Telescope images, which have revealed them to be supergiants (Aldering et al. 1994; Maund et al. 2011; Van Dyk et al. 2014). In some cases, however, the progenitor radii estimated from SCE modeling are in tension with those measured from direct imaging (e.g., Arcavi et al. 2017; Tartaglia et al. 2017, in the case of SN 2016gkg;). Potential binary companions to the progenitor, which have been observed or inferred in a handful of cases (e.g., Maund et al. 2004; Benvenuto et al. 2013) can further complicate direct imaging estimates when the individual binary members are unresolvable.

Here, we present photometric and spectroscopic observations of SN 2020bio, an SN IIb showing remarkably strong early-time emission, obtained by Las Cumbres Observatory (LCO) through the Global Supernova Project (GSP). LCO extensively observed SN 2020bio from hours to $\approx$160 days after explosion, providing a detailed look into the full evolution of a double-peaked SN IIb. In this work, we analyze its light-curve evolution and spectral features, and we fit analytic models to its full light-curve evolution to estimate the radius, mass, and structure of its progenitor star. We also compare its bolometric light curve and spectra to numerical models in order to infer its progenitor mass and the properties of its circumstellar environment.

This paper is organized as follows. In Section 2, we describe the discovery and follow-up observations of SN 2020bio. We present its full light-curve and spectral time series in Section 3, and we compare observations to analytical and numerical models in Section 4. Finally, in Section 5, we discuss the potential progenitor properties of SN 2020bio given the presented evidence.

2. Discovery and Data Description

SN 2020bio was discovered by Koichi Itagaki on UT 2020 January 29.77 at the Itagaki Astronomical Observatory at an unfiltered Vega magnitude of 16.7. Stacking images of the same field obtained by the Asteroid Terrestrial-impact Last Alert System (ATLAS) survey on the previous night yield a nondetection down to c-band magnitude 20.6. Soon after discovery, rapid photometric and spectroscopic follow-up observations were requested by the GSP through the Las Cumbres global network of telescopes. The GSP also triggered its Swift Key Project (1518618: PI Howell) to obtain daily UV and optical photometry. A classification spectrum obtained on the 2.0 m Liverpool Telescope on 2020 January 31.19—approximately 1.5 days after the first detection—shows a blue continuum superimposed with a narrow Hα emission feature and a broad possible He I λ 5876 Å feature, consistent with a young core-collapse SN (Srivastav et al. 2020).

SN 2020bio exploded at R.A. $13^{\rm h}\,55^{\rm m}37\overset{\rm s}{.}69$ and decl. $+40°\,28'39\overset{''}{.}1$ in the spiral galaxy NGC 5371 at redshift $z = 0.008533$ (Springob et al. 2005). The distance to NGC 5371 is uncertain due to its low redshift. We adopt the mean of several distances measured using the method of Tully & Fisher (1977), which gives $d = 29.9 \pm 5.1$ Mpc (values from the NASA Extragalactic Database[17]). Using the Schlafly & Finkbeiner (2011) dust map calibrations, we estimate a Galactic line-of-sight extinction to SN 2020bio $E_{\rm MW}(B-V) = 0.008$ mag. Given the location of SN 2020bio with respect to its host galaxy, we also estimate host extinction using the Na I D equivalent widths measured in a high-resolution spectrum of the SN. From the conversions presented in Poznanski et al. (2012), we estimate $E_{\rm host}(B-V) = 0.068 \pm 0.038$ mag for a total extinction $E(B-V) = 0.076 \pm 0.038$ mag. The photometry of SN 2020bio presented throughout this work is corrected for this mean total extinction.

LCO photometric follow-up commenced less than a day after discovery. *UBgVri*-band images were obtained by the Sinistro and Spectral cameras mounted on LCO 1.0 and 2.0 m telescopes, respectively, located at McDonald Observatory, Teide Observatory, and Haleakala Observatory. Data were

[17] https://ned.ipac.caltech.edu/

Table 1
UV and Optical Photometry

JD	Filter	Magnitude	Uncertainty	Source
2458878.27	Clear	16.77	0.15	Itagaki
2458878.33	Clear	16.55	0.15	Itagaki
2458878.39	Clear	16.51	0.15	Itagaki
2458879.27	Clear	16.22	0.15	Itagaki
2458880.26	Clear	16.49	0.15	Itagaki
2458881.25	Clear	16.68	0.15	Itagaki
2458882.18	Clear	16.82	0.15	Itagaki
2458883.26	Clear	16.85	0.15	Itagaki
2458878.85	UVW2	13.56	0.04	Swift
2458879.89	UVW2	14.59	0.05	Swift

(This table is available in its entirety in machine-readable form.)

reduced using `lcogtsnpipe` (Valenti et al. 2016), which extracts point-spread function magnitudes after calculating zero points and color terms (Stetson 1987). *UBV*-band photometry was calibrated to Vega magnitudes using Landolt standard fields (Landolt 1992), while *gri*-band photometry was calibrated to AB magnitudes (Smith et al. 2002) using Sloan Digital Sky Survey (SDSS) catalogs. As SN 2020bio exploded coincident with its host galaxy, to remove host galaxy light we performed template subtraction using the HOTPANTS (Becker 2015) algorithm and template images obtained after the SN had faded. Unfiltered images were obtained with the Itagaki Astronomical Observatory (Okayama and Kochi, Japan) 0.35 m telescopes + KAF-1001E (CCD). Using our custom software, the photometry was extracted after host subtraction and calibrated to the *V*-band magnitudes of 45 field stars from the Fourth US Naval Observatory CCD Astrograph Catalog (Zacharias et al. 2013).

We also obtained ATLAS (Tonry et al. 2018; Smith et al. 2020) forced photometry from the forced photometry server (Shingles et al. 2021). Images obtained on the same night were averaged for higher signal-to-noise ratios. Magnitudes in the *c* and *o* bands were calibrated to AB magnitudes.

UV and optical photometry were obtained with the Ultraviolet and Optical Telescope (UVOT; Roming et al. 2005) on the Neil Gehrels Swift observatory (Gehrels et al. 2004). Swift data were reduced using a custom adaptation of the Swift Optical/Ultraviolet Supernova Archive (Brown et al. 2014) pipeline with the most recent calibration files and the zero points of Breeveld et al. (2011). Images from the final epoch, obtained after the SN had sufficiently faded, were used as templates to subtract the host galaxy light. All Swift photometry is calibrated to Vega magnitudes. The entire UV and optical data sets from LCO, Itagaki, and Swift UVOT are given in Table 1 and shown in Figure 1.

LCO spectra were obtained by the FLOYDS spectrograph on the 2.0 m Faulkes Telescope North at Haleakala Observatory. Spectra cover a wavelength range of 3500–10,000 Å at a resolution $R \approx 300$–600. Data were reduced using the `floydsspec` pipeline,[18] a custom pipeline, which performs cosmic ray removal, spectrum extraction, and wavelength and flux calibration. We also present one spectrum obtained by the B and C spectrograph on the 2.3 m Bok Telescope at Steward Observatory, two spectra obtained by the Blue Channel Spectrograph on the 6.5 m MMT at the Fred Lawrence Whipple Observatory, and one spectrum obtained by the Optical System for Imaging and low/intermediate-Resolution Integrated Spectroscopy (OSIRIS) spectrograph on the 10.4 m Gran Telescopio Canarias. Details of all these spectra are presented in Table 2.

[18] https://github.com/svalenti/FLOYDS_pipeline/

3. Photometric and Spectral Analysis

3.1. Spectroscopic Classification

Given the unusual features of SN 2020bio compared to SNe IIb in literature (see Sections 3 and 4), as well as the lack of a public classification, here we attempt to accurately classify SN 2020bio. Analyzing the spectra of SN 2020bio using SN classification software (Howell et al. 2005; Blondin & Tonry 2007) gives matches to both SNe IIb and SNe Ib. At early times, more matches are found to SNe IIb, in particular the prototypical Type IIb SN 1993J, than other classes (12 of 19 top `SNID` matches), while at later times, the matches are split more evenly. To explore the classification at this phase in greater detail, we compare the spectrum of SN 2020bio 26 days after explosion with the mean Type Ib and Type IIb spectra from Liu et al. (2016) in Figure 2. As Hα is one of the distinguishing features between SNe IIb and SNe Ib, we focus on this region of the spectra in the inset. SN 2020bio lacks the strong, broad emission that is commonplace in most SNe IIb spectra. However, it also does not match the strong He I λ 6678 P Cygni feature that is seen in SNe Ib.

We consider two possibilities to explain the observed features in this region of the spectrum. First, it may consist mainly of broad but weak Hα emission with a superimposed narrow host emission line. An absorption feature just blueward of that host line may be He λ 6678 absorption, as seen in other "flat-topped" Hα features in SNe IIb. Assuming this absorption is from He, we measure an ejecta velocity of $\approx$7500 km s^{-1}. This velocity also corresponds to other absorption features seen in the spectrum corresponding to He I λ 5876 and He I λ 7065.

The second possibility is that this region of the spectrum is dominated by a P Cygni feature of He I λ 6678. In this case, the He absorption from this P Cygni feature gives an ejecta velocity of $\approx$14,000 km s^{-1}. The narrow absorption just blueward of the narrow Hα is more difficult to explain. One potential source is absorption by circumstellar H. The velocity of the absorption minimum relative to Hα is $\approx$1000 km s^{-1} —faster than typical red supergiant or yellow supergiant winds (Smith 2014) but not unreasonable if the CSM is accelerated by interaction with the SN ejecta. Circumstellar interaction may also contribute to the narrow Hα emission feature. While inspecting the 2D FLOYDS spectrum reveals residual Hα contamination from the host galaxy, analyzing the full width at half maximum of this line over the first three weeks after explosion reveals a decreasing trend. Therefore, we cannot rule out circumstellar interaction as a contribution to the narrow H P Cygni feature.

Other diagnostics to differentiate between SNe IIb and Ib include the time evolution of the pseudo-equivalent width (pEW) of the Hα absorption and the absorption velocity of the He I λ 5876 feature. Liu et al. (2016) show that both classes occupy relatively distinct regions of these parameter spaces. Here, we follow their methodology to measure both the Hα pEW and the He I absorption velocity in the spectra of SN 2020bio beginning at the second *V*-band peak. The results are plotted in Figure 3 along with the Liu et al. (2016) sample.

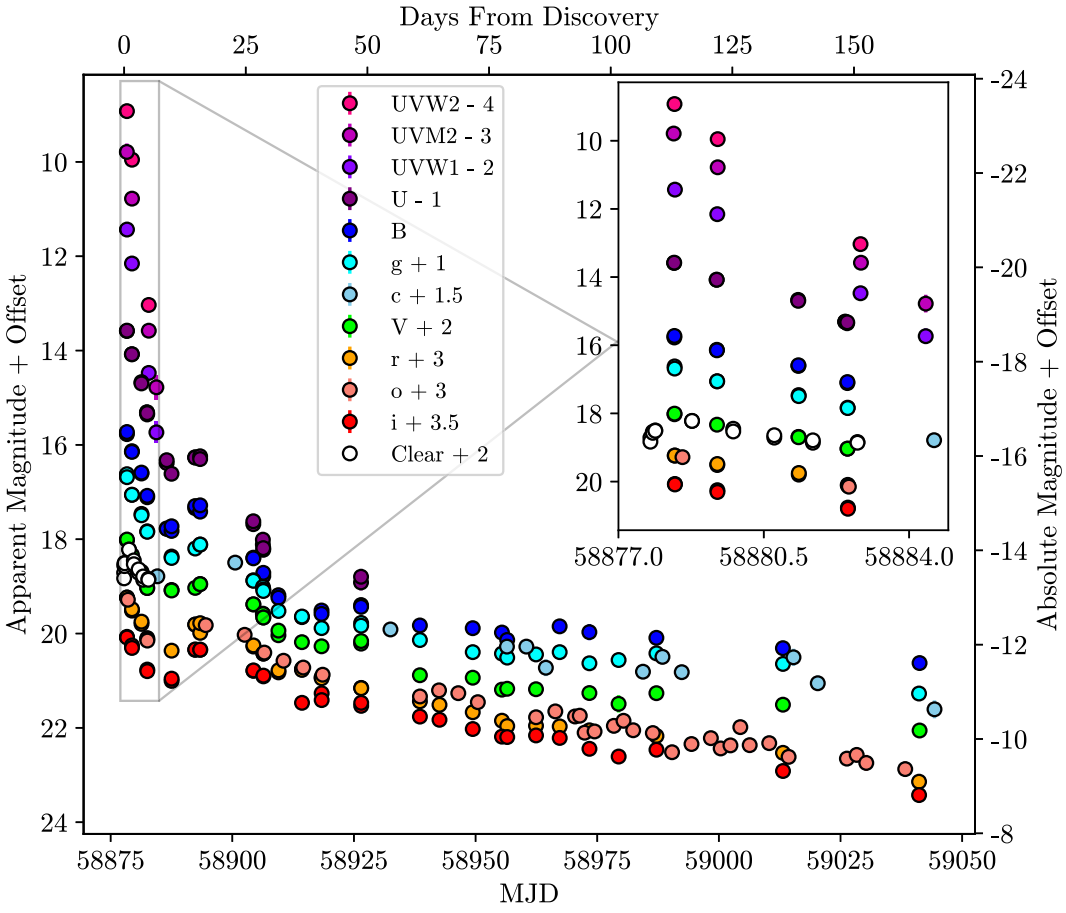

Figure 1. The full extinction-corrected light curves of SN 2020bio. Photometry in different filters have been offset for clarity. Unfiltered photometry from the Itagaki Astronomical Observatory is included as clear points and calibrated to the *V* band. The inset focuses on the rapidly evolving shock-cooling emission.

Table 2
Log of Spectroscopic Observations

Date of Observation	Days since Discovery	Facility/Instrument	Exposure Time (s)	Wavelength Range (Å)
2020-01-31 04:27:31	1	LT/SPRAT	1200	4000–7925
2020-02-03 14:32:18	4	LCO/FLOYDS-N	1800	3500–10,000
2020-02-05 12:19:05	6	LCO/FLOYDS-N	1800	3500–10,000
2020-02-15 09:35:59	16	Bok/B &C	600	3850–7500
2020-02-18 12:32:26	19	MMT/Blue Channel	300	5700–7000
2020-02-24 13:00:37	25	LCO/FLOYDS-N	1800	3500–10,000
2020-03-03 10:49:44	33	LCO/FLOYDS-N	2700	3500–10,000
2020-03-22 14:22:56	52	LCO/FLOYDS-N	3600	3500–10,000
2020-03-30 14:20:34	60	LCO/FLOYDS-N	3600	3500–10,000
2020-04-16 11:12:12	77	LCO/FLOYDS-N	3600	3500–10,000
2020-04-27 12:09:24	88	LCO/FLOYDS-N	3600	3500–10,000
2020-08-18 22:02:01	201	GTC/OSIRIS	1500	3600–7808

Note. All spectra will be made publicly available on WiseRep (Yaron & Gal-Yam 2012).

Again, SN 2020bio appears to be a transitional object, with similar pEW values to both SNe IIb and Ib. However, it also has much lower He I absorption velocities than almost all the SNe Ib, in particular at late times. This is consistent with the conclusions of Liu et al. (2016), who found that SNe IIb have systematically lower absorption velocities than SNe Ib throughout their evolution.

In summary, the classification of SN 2020bio is difficult to determine with high confidence. The spectra reveal that this object is unique—emission from H-rich ejecta is very weak or nonexistent, and circumstellar interaction may be contributing to the peculiar spectral features. If there is weak but broad H emission, then the outer layers of the progenitor may have been almost entirely stripped of the H-rich material, placing SN 2020bio in a transitional region between SNe IIb and SNe Ib. On the other hand, if the ejecta is H-free, then SN 2020bio is a very rare example of an SN Ib with a double-peaked light curve. However, based on the emission centered

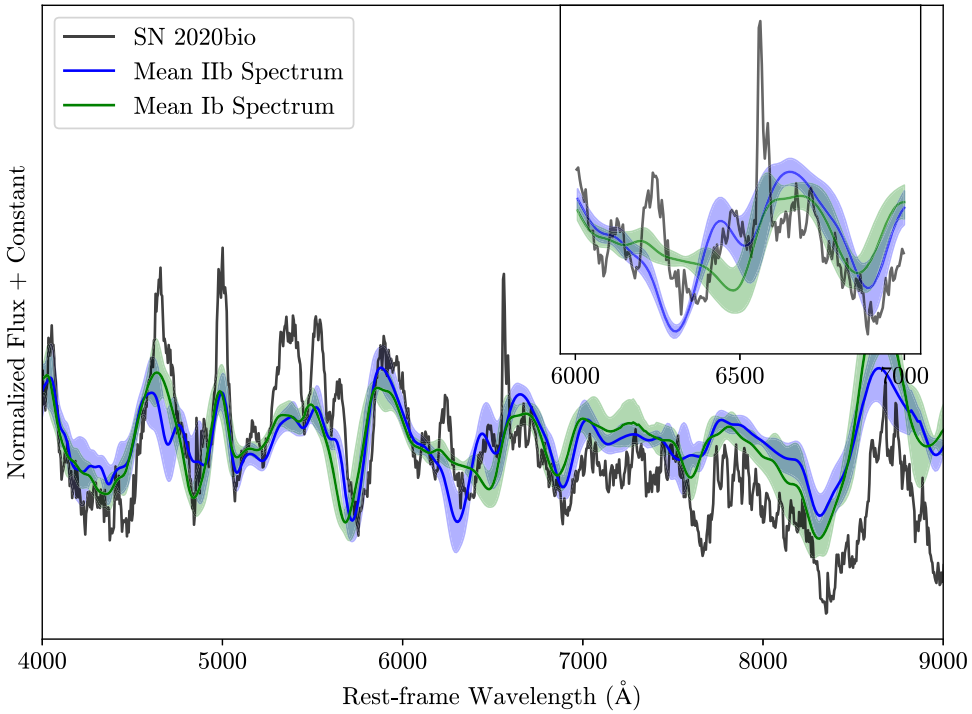

Figure 2. The spectrum of SN 2020bio ≈26 days after explosion, compared with the mean Type Ib and Type IIb template spectra (Liu et al. 2016) at the same phase. SN 2020bio has spectral features in common with both these classes. The inset shows the region surrounding the Hα line. SN 2020bio has a weak and broad Hα emission feature that is weaker than that in the mean SN IIb spectrum. However, this feature is much different than those seen in typical SNe Ib. This may indicate that the progenitor of SN 2020bio was stripped almost entirely of its H-rich envelope.

Table 3
SCE Model Parameters

Model	$R_{\rm env}$ ($R_\odot$)	$M_{\rm env}$ ($10^{-2}\ M_\odot$)	v^a (10^4 km s^{-1})	t_0 (days)	χ^2 / d.o.f.
P15	510^{+30}_{-30}	$1.14^{+0.02}_{-0.02}$	$1.67^{+0.02}_{-0.01}$	$0.67^{+0.02}_{-0.02}$	21.6
P21	1700^{+85}_{-95}	$1.60^{+0.03}_{-0.02}$	$1.36^{+0.01}_{-0.02}$	$0.98^{+0.01}_{-0.01}$	21.1
SW17 ($n = 3/2$)	160^{+12}_{-10}	$47.12^{+0.96}_{-0.92}$	$1.69^{+0.04}_{-0.04}$	$0.26^{+0.04}_{-0.04}$	8.7
SW17 ($n = 3$)	220^{+19}_{-15}	$322.60^{+6.10}_{-6.20}$	$1.60^{+0.04}_{-0.04}$	$0.25^{+0.04}_{-0.04}$	8.7

[a] **Note.** The characteristic velocity for P15 and P21 and the shock velocity for SW17.

around ≈6550 Å that is broader than seen in typical SN Ib spectra, as well as the consistent ejecta velocity measurements of ≈7500 km s^{-1}, we favor the former interpretation. The close match to the SN IIb template, albeit with weak but broad Hα, allows us to classify this object as an SN of Type IIb.

3.2. Light Curve and Color Evolution

In Figure 1, we show the full LCO, ATLAS, and Swift extinction-corrected light curve of SN 2020bio, from detection to ≈160 days after explosion. The discovery and subsequent follow-up photometry from Itagaki are included as "Clear" data points. The inset shows in greater detail the early-time evolution of the SCE, focusing on the first week after discovery. The most distinctive feature of the light curve is the luminous and rapidly declining SCE at early times. The peak SCE luminosity exceeds that of the secondary peak ≈15 days later, but SCE only dominates the light curve during the first several days. Over this time, the light curve falls by ≈4 mag in the first week, making this phase difficult to observe without rapid multiwavelength follow-up.

After ≈4 days from discovery, the slope of the light-curve decline changes as the luminosity from ^{56}Ni decay begins to dominate the light curve. After about a week, the light curve rebrightens and reaches a secondary maximum ≈15 days after discovery. From this point, the emission settles onto the radioactive decay tail, powered by ^{56}Co decay, for the remainder of the observations. The secondary peak and overall late-time light curve is relatively dim, peaking at $M \approx -14$ mag in the V-band, hinting at a small amount of ^{56}Ni synthesized in the explosion.

In Figure 4, we compare the early-time UV-optical colors of SN 2020bio to those of other SNe IIb with observed SCE in the UV. The B- and V-band data for all the objects, with the exception of SN 2010jr, consist of ground-based photometry in order to avoid uncertain subtractions and calibrations in Swift optical bands. All dates are given with respect to the time of discovery and corrected for extinction according to the published values for each object. SN 2020bio has both the earliest observations relative to discovery and the bluest colors throughout its evolution compared to the other objects. While objects such as SN 2010jr and SN 2016gkg have more densely sampled light curves, their observations began later and their colors evolved redward faster compared to SN 2020bio. Of the six colors plotted, SN 2020bio is exceptionally blue in the *UVM2-B* and *UVM2-V* colors, in particular in the earliest epochs. This may be evidence for another luminosity contribution besides SCE, as we discuss in Section 5.

3.3. Spectral Comparison

Spectral coverage of SN 2020bio began fewer than 2 days after the first detection—approximately 3 days since the estimated explosion time (Section 4.2)—and continued for

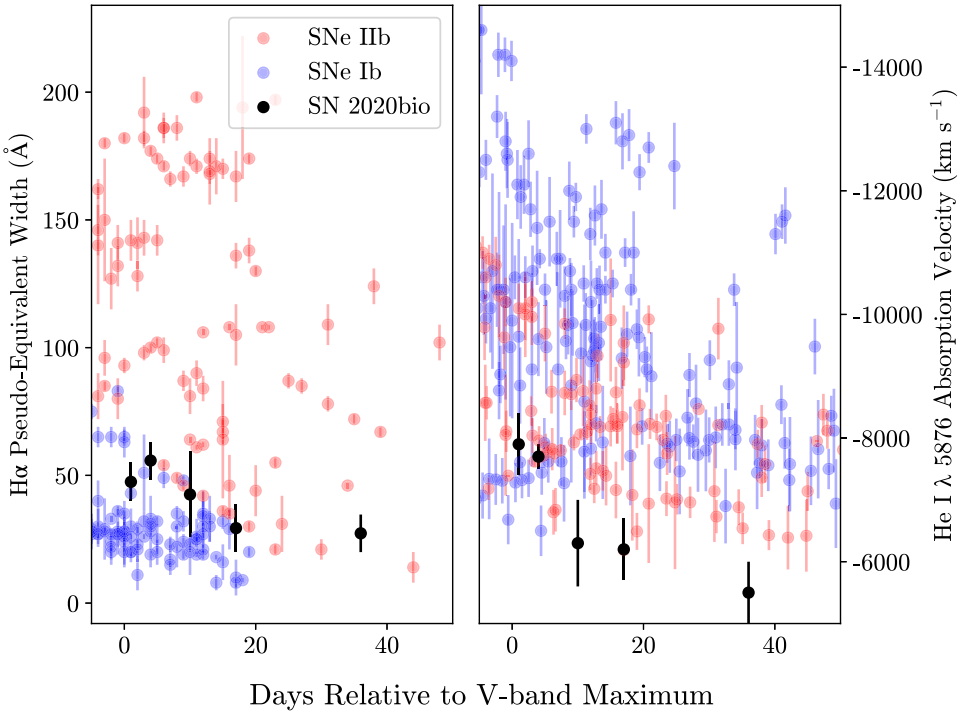

Figure 3. The evolution of the Hα pseudo-equivalent width (left) and the He I λ 5876 absorption velocity (right) of SN 2020bio (black) compared to SNe IIb (red) and Ib (blue) from Liu et al. (2016). SN 2020bio has values that are consistent with the relative extremes of both classes of objects but is more similar at later times to SNe IIb, in particular in its absorption velocities.

201 days. We plot the full spectral series in Figure 5. The earliest spectrum of SN 2020bio, reported to the Transient Name Server (Srivastav et al. 2020), shows a hot blue continuum superimposed with weak emission features. We identify a potential weak, broad feature of He I λ5876 Å blueshifted by $\approx$11,000 km s^{-1}. We also note potential narrow lines of Hα and Hβ; however, these features are consistent with host galaxy contamination at the resolution of the spectrum.

After about a week after the explosion, absorption features begin to develop in the spectra. We identify lines of He, O, and Ca. The absorption feature blueward of the rest-frame Hα line matches He I λ 6678 Å absorption blueshifted by $\approx$7500 km s^{-1}, which is commonly noted to cause "flat-topped" Hα emission profiles in other SNe IIb (e.g., Filippenko et al. 1993). In general, the absorption features in the SN 2020bio spectra are shallower than those of the other SNe IIb, in particular SN 2011dh. Interaction with CSM can produce absorption features that are weaker and shallower than expected, which has been noted in the spectra of SN 1993J and SN 2013df (Fremling et al. 2019).

To further investigate the differences between SN 2020bio and other SNe IIb, in Figure 6 we plot comparison spectra just after (top), two weeks after (middle), and three weeks after (bottom) explosion. Among this sample, many of the other SNe IIb show broadened, high-velocity H and He features at early times. However, the spectrum of SN 2020bio at this same phase shows only a blue continuum with possible weak He I emission. This difference suggests that the photosphere has not yet receded within the outermost ejecta. One explanation for this is if the SN ejecta is surrounded by low-density CSM. At this phase, any narrow lines caused by photoionization or collisional excitation may have vanished, but the photosphere could still lie within this shock-heated material, obscuring the ejecta features within. By the time of our next spectrum (4 days after discovery) the photosphere has receded into the SN ejecta, revealing broad SN features. Narrow lines also persist in the spectra of SN 2020bio; however, these are at least partially due to galaxy contamination, as `floydsspec` does not remove host galaxy contamination during the reduction.

Differences persist weeks after the estimated explosion times. While the other SNe IIb have developed broad Hα and Hβ emission features, these same lines are weaker in SN 2020bio. This could be partly caused by He I λ 6678 Å absorption, which has an absorption trough coincident with the Hα flux when blueshifted by $\approx$7500 km s^{-1}. Another possibility, as mentioned in Section 3.1, is that the H emission from SN 2020bio is inherently weaker than in other SNe IIb, which may be the case if the progenitor lost more of its outer H-rich envelope than the progenitors of the other SNe IIb did. Weak H emission, along with potential CSM, point to a scenario in which the progenitor of SN 2020bio underwent enhanced mass loss, shedding almost all of its outer H layer before exploding. If this is the case, such a progenitor scenario for SN 2020bio is unique among other well-studied SNe IIb.

4. Light-curve Modeling and Progenitor Inference

4.1. Shock-cooling Model Descriptions

A variety of analytical and numerical models of SCE have been developed in recent years. Here, we consider three analytical models that are commonly used to fit the early-time emission of core-collapse SNe. The P15 model extends the formalism of Nakar & Piro (2014) to reproduce the full shock-cooling peak. It assumes a lower-mass extended envelope without assuming its specific density structure. On the other hand, SW17 calibrates to the numerical models of Rabinak & Waxman (2011) and assumes specific polytropic indices for the extended envelope. The methodology used to fit these models

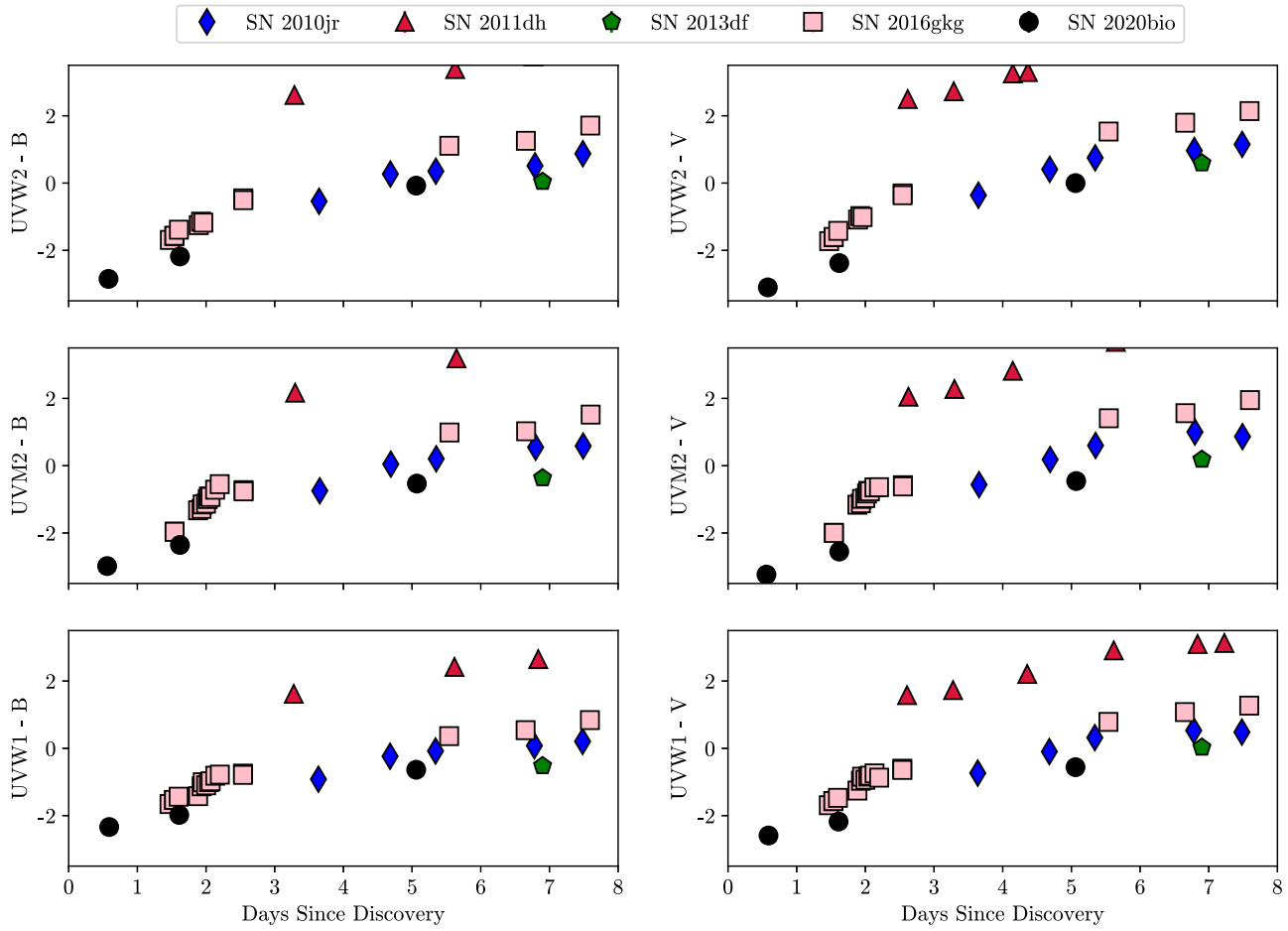

Figure 4. UV-optical colors of SN 2020bio compared with those of other SNe IIb with early-time Swift observations. SN 2020bio was bluer at earlier phases than the other SNe IIb. Data for these comparison SNe were obtained from the following sources: Arcavi et al. (2011) (SN 2011dh), Morales-Garoffolo et al. (2014) (SN 2013df), Arcavi et al. (2017) (SN 2016gkg), Pritchard et al. (2014) and the Open Astronomy Catalog (SN 2010jr), and this work (SN 2020bio).

to the data and derive resulting blackbody properties are presented in Arcavi et al. (2017).

More recently, Piro et al. (2021) developed another analytical model to better reproduce the early SCE observed in a variety of transients (e.g., Arcavi et al. 2017; Yao et al. 2020). They assume a two-zone extended envelope in homologous expansion and calculate the emission from this shocked material. This method begins by assuming extended material in homologous expansion separated into two regions —an outer density profile described by $\rho \propto r^{-n}$, where n $\approx$10, and an inner region with $\rho \propto r^{-\delta}$, where $\delta \approx$1.1. Assuming a transitional velocity v_t between the inner and outer regions of the extended material, the time for the diffusion front to reach this transition is given by

$$t_d = \left(\frac{3\kappa K M_e}{(n-1)v_t c}\right)^{1/2}, \quad (1)$$

where $K = \frac{(n-3)(3-\delta)}{4\pi(n-\delta)}$, κ is the optical opacity, and M_e is the mass of the extended material. The luminosity from the cooling of the extended material is then defined piecewise for times before and after this diffusion time:

$$L(t) \approx \frac{\pi(n-1)}{3(n-5)}\frac{cR_e v_t^2}{\kappa}\left(\frac{t_d}{t}\right)^{4/(n-2)}, \; t \leqslant t_d \quad (2)$$

and

$$L(t) \approx \frac{\pi(n-1)}{3(n-5)}\frac{cR_e v_t^2}{\kappa}\exp\left[-\frac{1}{2}\left(\frac{t^2}{t_d^2}-1\right)\right], \; t \geqslant t_d. \quad (3)$$

To fit the photometry in each band, we assume that the material radiates as a blackbody at some photospheric radius $r_{\rm ph}$. The photosphere reaches the transition between the two regions at a time

$$t_{\rm ph} = \left[\frac{3\kappa K M_e}{2(n-1)v_t^2}\right]^{1/2}, \quad (4)$$

and the time evolution of the photospheric radius is given relative to this characteristic time:

$$r_{\rm ph}(t) = \left(\frac{t_{\rm ph}}{t}\right)^{2/(n-1)} v_t t, \; t \leqslant t_{\rm ph} \quad (5)$$

and

$$r_{\rm ph}(t) = \left[\frac{\delta-1}{n-1}\left(\frac{t^2}{t_{\rm ph}^2}-1\right)+1\right]^{-1/(\delta-1)} v_t t, \; t \geqslant t_{\rm ph}. \quad (6)$$

In addition, we attempt to fit the analytical models of Shussman et al. (2016), which are calibrated to numerical simulations from shock breakout to recombination. However,

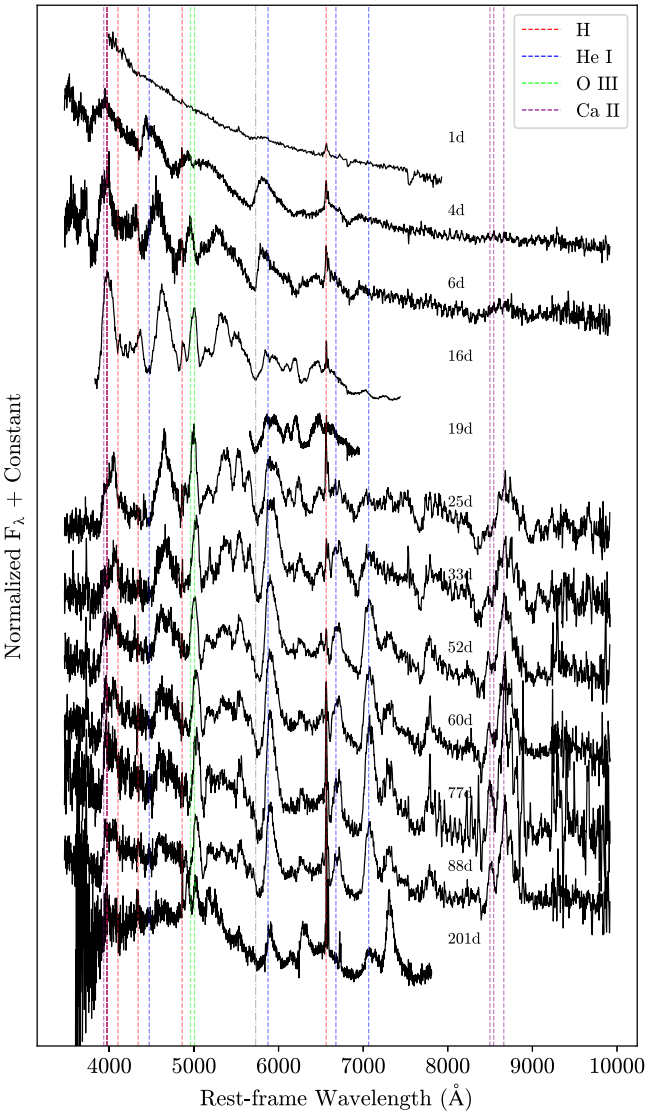

Figure 5. The full spectral time series of SN 2020bio. Phases with respect to the detection epoch are given above each spectrum. Notable spectral features are identified with dashed lines. The gray dashed–dotted line shows a He I λ 5876 absorption velocity of 7500 km s^{-1} for reference. The first spectrum is the publicly available classification spectrum retrieved from the Transient Name Server.

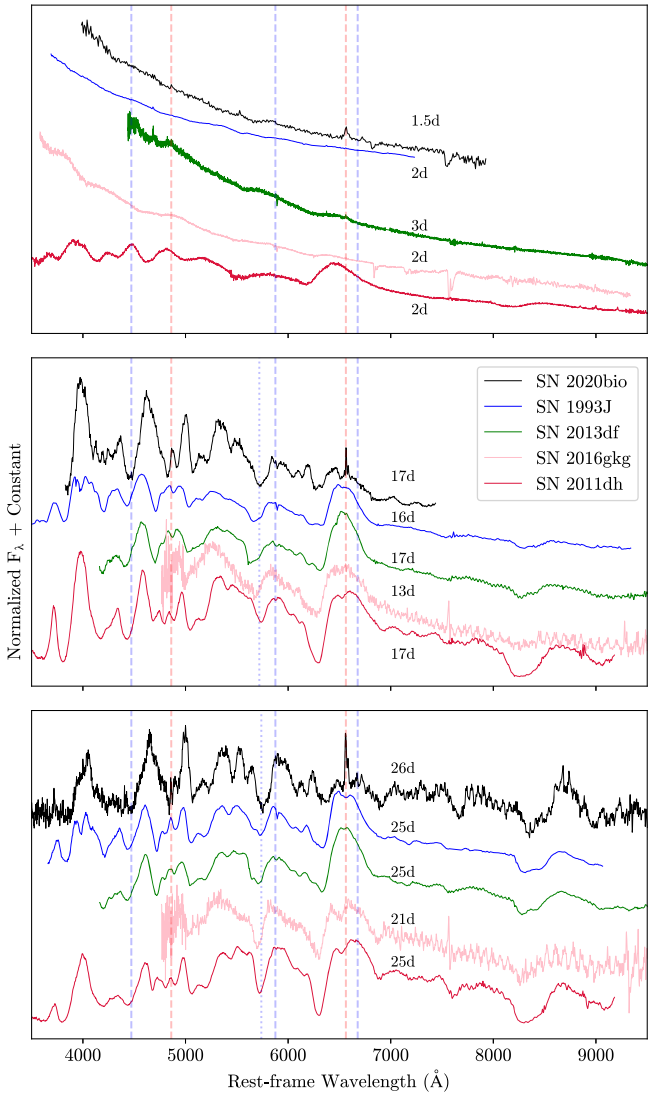

Figure 6. Spectra of SN 2020bio compared with spectra of other SNe IIb at similar phases. Phases with respect to the estimated explosion time are given above each spectrum, and notable spectral features are identified with red (H) and blue (He) vertical lines at their rest-frame wavelengths. The dotted line shows the He I λ 5876 absorption velocity of SN 2020bio. The spectra of SN 2016gkg are unpublished spectra obtained by LCO, while the other comparison spectra were retrieved from WiseRep (Yaron & Gal-Yam 2012).

these model fits are unable to reproduce the rapidly declining shock-cooling emission in all filters during the week after explosion. It is possible this shortcoming is due to an unphysical application of the model—which is calibrated to numerical simulations of red supergiants—to the early light curve of SN 2020bio, which likely had a different progenitor structure. Detailed comparisons between numerical models of SNe IIb and the Shussman et al. (2016) models are beyond the scope of this work.

4.2. Best-fit Analytic Models

We fit each model to the early-time photometry of SN 2020bio. For the SW17 model, we consider two polytropic indices ($n = 3/2$ and $n = 3$), appropriate for convective and radiative envelopes, respectively. Only data taken up to 3.5 days after discovery are fit, as this is the time when SCE dominates the luminosity over radioactive decay (see Section 4.3 for a quantitative treatment of the ^{56}Ni light curve). Additionally, we ensure that the phases we fit fall within the validity range of each model. In each case, we fit for the progenitor extended envelope radius, $R_{\rm env}$, the envelope mass, $M_{\rm env}$, either the characteristic velocity or the shock velocity v of the outer material, and the offset time since explosion t_0. We use the `emcee` package (Foreman-Mackey et al. 2013) to perform Markov Chain Monte Carlo fitting of each model, initializing 100 walkers with 1000 burn-in steps and running for an additional 1000 steps after burn-in. For each step, the total luminosity is computed using the analytical model formalism, and the luminosity within each filter is compared to the observed photometry assuming a blackbody spectral energy distribution (SED). We fit each model assuming an optical opacity $\kappa = 0.34$ cm^2 g^{-1}, consistent with solar-composition material.

The best-fit models to the multiband SCE light curves are shown in Figure 7, and best-fit parameters are given in Table 3 with corner plots shown in Appendix. The Itagaki discovery data that capture the rise are calibrated to the V band. We find that all

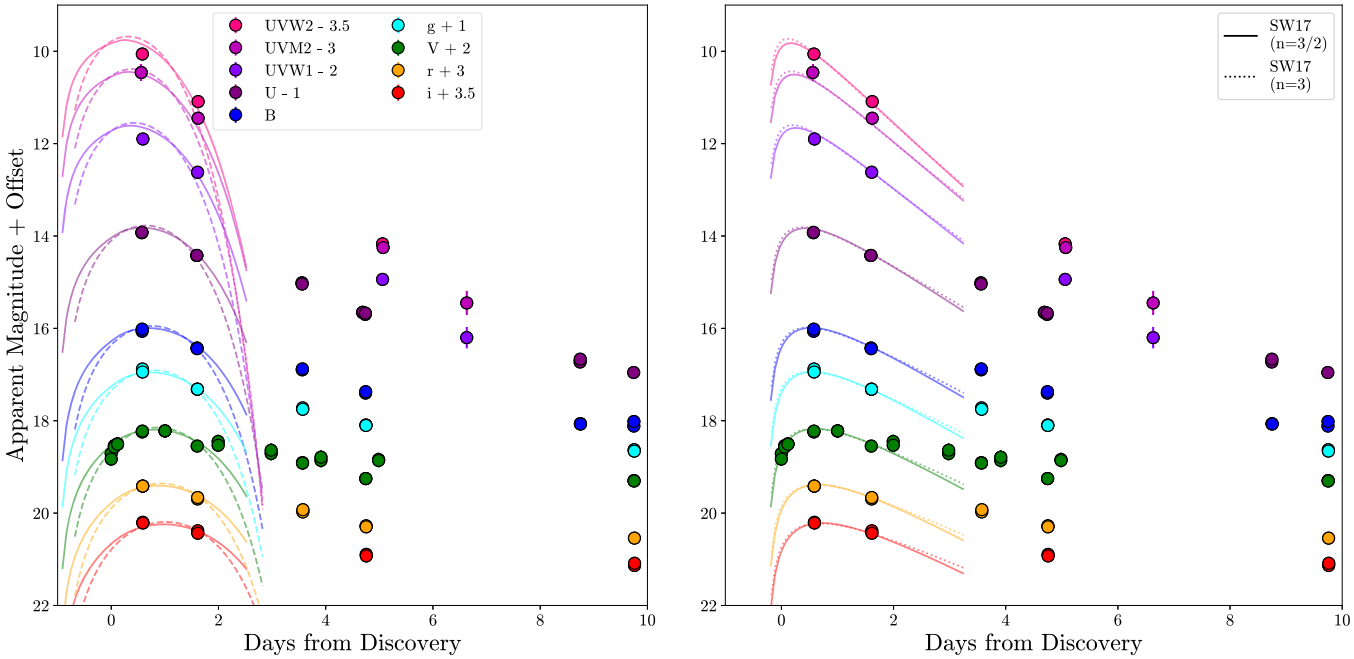

Figure 7. Shock-cooling fits to the early-time photometry of SN 2020bio using the models of (left) P15 and P21 and that of (right) SW17, assuming a constant optical opacity appropriate for solar-composition material. Photometry in each band has been offset for clarity. Itagaki discovery photometry has been included in the *V*-band fits.

the models fit the early-time data well, reproducing the rapid rise, luminous peak, and subsequent decline in all filters. Quantitatively, the SW17 model for convective envelopes ($n = 3/2$) has the lowest reduced χ^2 value, indicating the model most closely matches the observations. On the other hand, the best-fit envelope mass for the SW17 model with a radiative ($n = 3$) envelope is larger than the total ejecta mass, estimated in Section 4.3. Therefore, we do not consider this model representative of the progenitor of SN 2020bio.

Based on the unusual properties of SN 2020bio compared to other SNe IIb, including its weak H spectral features and faint secondary light-curve peak, we test whether a lower-opacity envelope better reproduces the observed SCE. This could be the case if the progenitor star was almost completely stripped of its outer H-rich envelope. We perform the same fitting routine but fix the opacity $\kappa = 0.20$ cm^2 g^{-1} for H-poor material. The results are shown in Figure A5, with best-fit parameter values given in Table A1. We find no differences in goodness of fits for each model between the two chosen opacities—both the H-rich and H-poor envelopes produce similarly good fits. However, there are differences in the fitted parameters between the best-fit models. In the H-rich case, the envelope radii and masses from the best-fit SW17 model are consistent with those estimated for other SNe IIb (i.e., radii of $\approx 1 \times 10^{13}$ cm and masses of 10^{-3}–10^{-2} $M_\odot$). In the H-poor case, however, the radii are smaller (≈ 100 $R_\odot$) and the envelope masses are larger (≈ 0.5 $M_\odot$). These values are more consistent with those estimated for Type Ib and Ca-rich transients with observed SCE (e.g., Yao et al. 2020; Jacobson-Galán et al. 2022).

4.3. Bolometric Luminosities and Numerical Modeling

SCE dominates the total luminosity only for several days after explosion. The rest of the light curve is powered by the radioactive decay of ^{56}Ni and its children isotopes. Using our multiband coverage of SN 2020bio for $\approx$160 days after explosion, we construct a pseudo-bolometric light curve to fit for the amount of ^{56}Ni produced in the explosion. For epochs with observations in more than three filters, we extrapolate the SED out to the blue and red edges of the *U*- and *i*-band filters, respectively, using a univariate spline. We choose to extrapolate the (extinction-corrected) photometry rather than fit a blackbody SED, because the spectra are not representative of a blackbody throughout the object's evolution.

To infer the properties of the pre-explosion progenitor as well as the explosion itself, we compare numerical MESA (Paxton et al. 2011, 2013, 2015, 2018, 2019) and STELLA (Blinnikov et al. 1998, 2000, 2006) model explosions to our pseudo-bolometric light curve. As no model from the grid of Hiramatsu et al. (2021) reproduces the weak secondary peak of SN 2020bio, we expand their model grid with higher wind efficiencies ($\eta = 5.05.2$). For the best-fit models presented here, we begin with a MESA single-star progenitor with zero-age main-sequence (ZAMS) mass $M_{\rm ZAMS} = 15$ $M_\odot$ at solar metallicity and evolve it to a final mass of 4.8 $M_\odot$ with a wind efficiency $\eta = 5.2$ and no rotation. At explosion, the progenitor has a H-rich envelope radius of 280 $R_\odot$ and mass of 0.10 $M_\odot$, in agreement with values we find from our best-fit H-rich SCE models. The explosion energy and ejecta mass are fixed at 0.9×10^{51} erg and 2.9 $M_\odot$, respectively, and the mass of ^{56}Ni ($M_{\rm Ni}$) is varied between 0.015 and 0.020 $M_\odot$. These explosion models are then run through STELLA using 600 spatial zones and 100 frequency bins in order to reproduce the bolometric luminosity evolution. For more information, see Hiramatsu et al. (2021). The MESA model files are available on Zenodo.[19]

The resulting model light curves are shown in Figure 8, compared with the pseudo-bolometric light curve of SN 2020bio. We find decent qualitative agreement between the numerical models and the observed light-curve evolution, in particular at later times. The secondary light-curve peak and

[19] doi:10.5281/zenodo.7927189

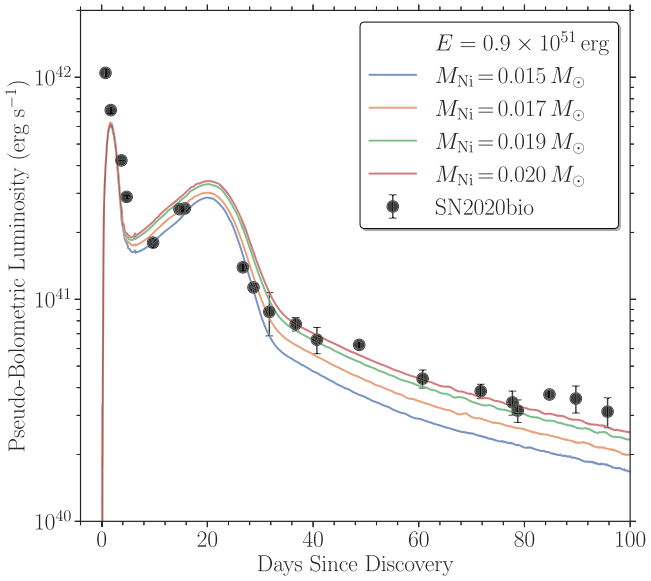

Figure 8. Numerical MESA and STELLA model light curves of SN 2020bio for varying $M_{\rm Ni}$. Both the secondary light-curve peak and late-time light-curve slope are best reproduced with $\approx$0.02 $M_\odot$ of ^{56}Ni synthesized in the explosion.

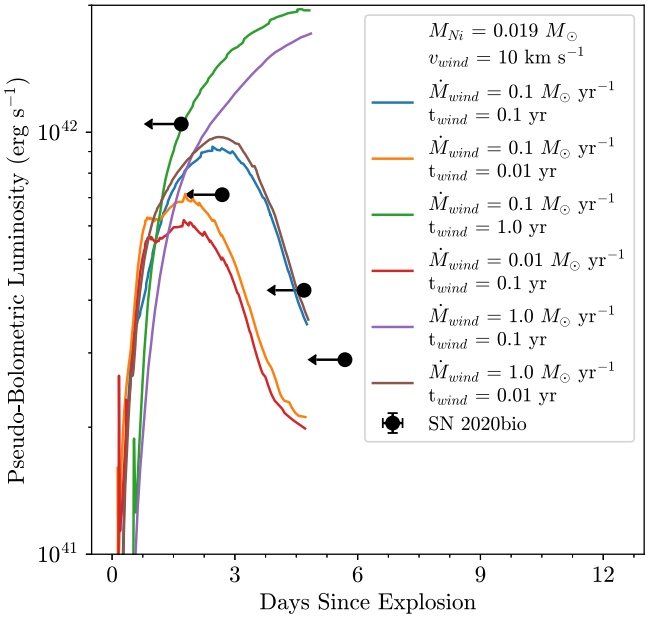

Figure 9. Numerical MESA and STELLA circumstellar interaction-powered model light curves of SN 2020bio at early times. Different color curves correspond to models with varying mass-loss rates and timescales. Leftward-facing arrows show the range of possible explosion epochs inferred from our SCE fits. The early-time emission excess is best reproduced with 0.001–0.01 $M_\odot$ of CSM.

late-time light-curve slope are well reproduced by an explosion that synthesizes $\approx$0.02 $M_\odot$ of ^{56}Ni. The secondary light-curve peak may be overproduced, but the exact peak luminosity and time of peak are uncertain, given the gap in our observational coverage.

Interestingly, however, the peak luminosity of the SCE is not reproduced by these models. It may be that the treatment of the SN shock and the subsequent cooling of the outer envelope is too complex to fully simulate within these models. On the other hand, it is possible that an additional powering mechanism contributes to the early-time evolution. To test this, we explore how the addition of different mass-loss rates and timescales to the models affects the early-time light curve through short-lived circumstellar interaction. To the best-fit MESA model, we attach a wind density profile $\rho_{\rm CSM}(r) = \dot{M}_{\rm wind}/4\pi r^2 v_{\rm wind}$, where $v_{\rm wind}$ = 10 km s^{-1}, with 100 additional spatial zones. These CSM models are shown in Figure 9. We find that the best-fit models have a confined CSM with masses of 1×10^{-3}–1×10^{-2} $M_\odot$ lost by the progenitor within the last several months before explosion. This hints that circumstellar interaction may contribute to the rapidly fading early-time emission of SN 2020bio and possibly other SNe IIb. If this is the case, then the information estimated through SCE model fits may not be truly representative of the true nature of their progenitors.

The values inferred from this numerical modeling, in particular the ^{56}Ni mass, are on the low end of the distribution of values estimated for other well-studied SNe IIb. SNe IIb with double-peaked light curves typically display secondary radioactive decay-powered peaks equally or more luminous than the peak of the SCE, implying a greater amount of ^{56}Ni synthesized. Studies using samples of these objects have found average ^{56}Ni masses of $\approx$0.10–0.15 $M_\odot$ and average ejecta masses of $\approx$2.2–4.5 $M_\odot$ (Lyman et al. 2016; Prentice et al. 2016; Taddia et al. 2018), in better agreement with ejecta parameters of other stripped-envelope and H-rich core-collapse SNe. However, rare cases of underluminous SNe IIb with low inferred $M_{\rm Ni}$ have been discovered (e.g., Nakaoka et al. 2019; Maeda et al. 2023). These objects have light curves that appear transitional between standard SNe II-P and SNe IIb, which differ from the observed photometric evolution of SN 2020bio.

On the other hand, in the case of SN 2018ivc, both a low ^{56}Ni mass ($M_{\rm Ni} \leqslant 0.015 M_\odot$) and progenitor mass ($M_{\rm ZAMS} \lesssim 12 M_\odot$) are inferred (Maeda et al. 2023). It is possible that other SNe IIb with little synthesized ^{56}Ni may be undercounted due to their rapidly fading or underluminous light curves. Maeda et al. (2023) also concluded that the light curve of SN 2018ivc was powered at least in part by circumstellar interaction. Sustained circumstellar interaction has been inferred for other SNe IIb, either through late-time spectral features (Maeda et al. 2015; Fremling et al. 2019) or through X-ray and radio observations (Fransson et al. 1996). It may be that the mechanism that produced the confined CSM inferred from our numerical models of SN 2020bio, and possibly that seen in the case of SN 2018ivc, points to more extreme mass loss than found in other SNe IIb.

4.4. Comparison to Nebula Spectra Models

A trend between an increasing amount of synthesized O and increasing core-collapse SN progenitor mass has been extensively studied (e.g., Woosley & Heger 2007). Jerkstrand et al. (2015) use this relationship to calibrate the [O I] $\lambda\lambda$ 6300,6364 luminosity, normalized by the radioactive decay luminosity at the same phase, with numerical models of SNe IIb progenitors (see Equation (1) of Jerkstrand et al. 2015). The authors consider models with zero-age main-sequence masses between 12 $M_\odot$ and 17 $M_\odot$. Comparing the observed normalized [O I] luminosity for a handful of SNe IIb, such as SN 1993J, SN 2008ax, and SN 2011dh, to these models allows for a direct estimate of their progenitor masses—all of which fall in the range of masses modeled.

Here, we reproduce this analysis using a nebular spectrum of SN 2020bio, obtained 201 days after the estimated explosion, shown in Figure 10. We estimate the luminosity from the [O I] $\lambda\lambda$

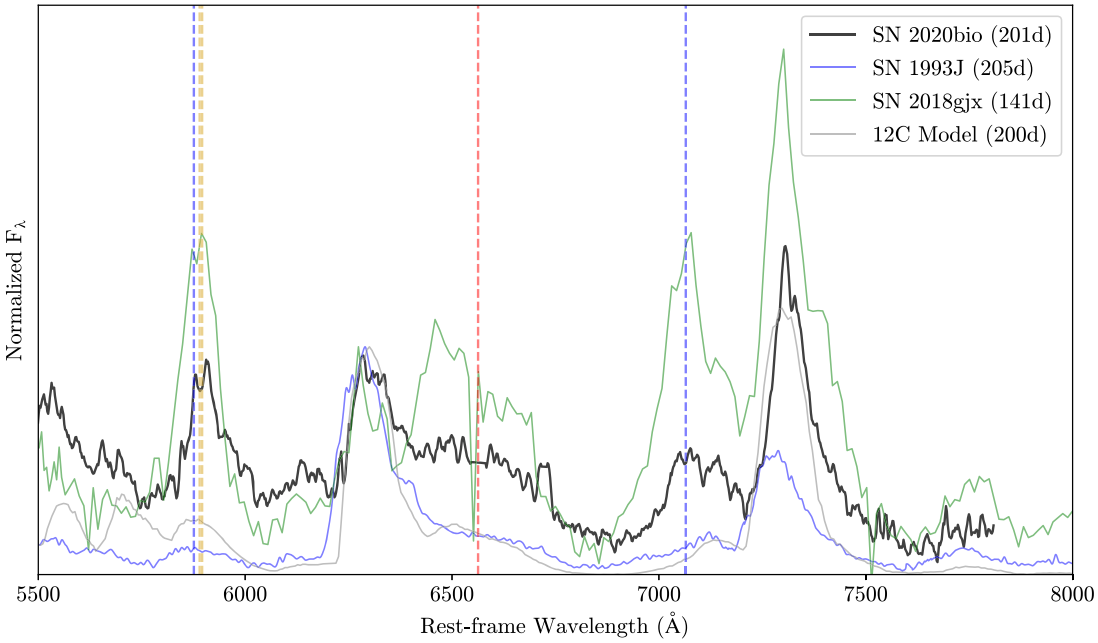

Figure 10. The nebular spectrum of SN 2020bio (black) compared to that of SN 1993J (blue), the 12C model of (Jerkstrand et al. 2015, gray), and the transitional Type IIb/Ibn SN 2018gjx (Prentice et al. 2020). Phases are given in the legend. Fluxes have been normalized to the [O I] emission feature, and galaxy emission lines have been masked for clarity. Notable features in the spectrum of SN 2020bio have been marked with dashed lines—Hα (red), He I λ 5876, λ 7065 (blue), and Na ID (gold).

6300,6364 emission doublet in the same way as Jerkstrand et al. (2015)—assuming the width of the feature to be 5000 km s^{-1}, we estimate the continuum by finding the minimum flux redward and blueward of this width and calculate the luminosity within the continuum-subtracted feature. We normalize this luminosity using the luminosity of ^{56}Ni decay, assuming the best-fit $M_{\rm Ni} = 0.019$ $M_\odot$ from Section 4.3.

The normalized luminosity at 201 days is $L_{\rm norm}(t = 201) = 9 \times 10^{-4} \pm 2 \times 10^{-5}$. This value is lower than any of the numerical models analyzed by Jerkstrand et al. (2015), implying a progenitor mass $\leqslant 12$ $M_\odot$. A low progenitor mass for SN 2020bio can also be inferred from the ratio of the [Ca II] $\lambda\lambda$ 7311, 7324 to [O I] $\lambda\lambda$ 6300, 6364 fluxes. A higher ratio implies a lower-mass progenitor, with SNe IIb from literature having values $\lesssim$1 throughout their nebular phases (e.g., Fang et al. 2019; Terreran et al. 2019; Hiramatsu et al. 2021). Using the same procedure as above, we estimate a [Ca II] to [O I] ratio of 1.34 ± 0.03—again pointing to a low-mass progenitor star.

Nebular spectroscopy has also been used to infer the presence of late-time circumstellar interaction in several SNe IIb, including SN 1993J (Fransson et al. 1996), SN 2013df (Maeda et al. 2015), and ZTF18aalrxas (Fremling et al. 2019). In these objects, interaction with H-rich material lost by the progenitor star was inferred through the presence of a boxy Hα profile that strengthened with time. While the origin of this feature at times $\lesssim$300 days after explosion is debated (e.g., Fang & Maeda 2018), Fremling et al. (2019) show that this feature is visible as early as $\approx$180 days after explosion. To search for signatures of interaction, in Figure 10 we compare the nebular spectrum of SN 2020bio with that of SN 1993J from a similar phase, the 12C model from Jerkstrand et al. (2015), and the interacting Type IIb/Ibn SN 2018gjx (Prentice et al. 2020). The host galaxy emission lines have been masked in the spectrum of SN 2020bio and all spectra have been normalized to the strength of the [O I] emission feature. The relative strength of the [O I] and [Ca II] features of SN 2020bio is reproduced well by this model, again supporting a $\approx$12 $M_\odot$ zero-age main-sequence progenitor.

At this phase, SN 2020bio exhibits several unusual features. An excess redward of the [O I] $\lambda\lambda$ 6300,6364 feature relative to the 12C model can be attributed to Hα powered by circumstellar interaction (Maeda et al. 2015; Fremling et al. 2019). While this feature may be due to [N II] (Jerkstrand et al. 2015), Fremling et al. (2019) found that ZTF18aalrxas still showed an excess even after subtracting off numerical models of SN IIb nebular spectra at this phase. More intriguing are two additional features centered around the He I λ 5876 and He I λ 7065 lines. These features are not found in the 12C model spectrum; however, they are of comparable width (albeit weaker in intensity) to the He I lines found in the nebular spectrum of SN 2018gjx. Prentice et al. (2020) claim that these lines are due to persistent interaction with He-rich circumstellar material that is revealed after the SN photosphere has receded sufficiently far into the ejecta. It is interesting to note that SN 2020bio and SN 2018gjx share several characteristics, including: Hα P Cygni features that are weaker than that of SN 1993J roughly 20 days after explosion; strong shock-cooling emission and a weak secondary light-curve peak, with similar amounts of ^{56}Ni produced; and weak [O I] compared to [Ca II] in their nebular spectra.

Based on its low synthesized ^{56}Ni mass and nebular spectral features, we conclude that SN 2020bio was likely the core collapse of a star with a lower mass than the progenitors of most other SNe IIb surrounded by an unusually massive CSM at the time of explosion.

5. Discussion and Conclusions

We have presented rapid multiband photometric and spectroscopic observations of SN 2020bio, a Type IIb SN with luminous and rapidly evolving SCE, beginning $\leqslant$ 1 day after explosion. Compared with other well-observed SNe IIb,

SN 2020bio has the bluest colors at early times as well as weak H spectral features throughout its evolution. Fitting analytical models of SCE to the early-time light curve gives progenitor radii on the order of 100 $R_\odot$–500 $R_\odot$ and envelope masses of 0.01 $M_\odot$–0.5 $M_\odot$ for our best-fit models, which are slightly greater than values derived for other SNe IIb progenitors using the same methods (e.g., SN 2016gkg; Arcavi et al. 2017). The weak secondary peak powered by radioactive decay is evidence of relatively little ^{56}Ni synthesized, $M_{\rm Ni} \approx 0.02\ M_\odot$, which is in tension with average $M_{\rm Ni}$ estimates from samples of other SNe IIb. Numerical modeling of the progenitor explosion within confined circumstellar material is consistent with the observed light curve, showing that circumstellar interaction is likely needed to reproduce the complete pseudo-bolometric light curve. Finally, comparing the nebular spectra to numerical models implies a progenitor ZAMS mass $\leqslant 12\ M_\odot$ and reveals signatures of interaction over 200 days after explosion.

It is difficult to explain all these peculiar features of SN 2020bio in one consistent model. The combination of its blue colors, spectral features, and our numerical modeling points to interaction with confined CSM that was stripped from the progenitor's outer envelope during the months prior to explosion. The best-fit progenitor parameters, in particular the large envelope radius and low envelope mass, may suggest an inflated progenitor undergoing enhanced mass-loss immediately before exploding. However, the very low ^{56}Ni and ejecta masses inferred from the later-time light curve, as well as the nebular spectroscopy, point to a lower-mass progenitor. It is possible that SN 2020bio was the collapse of an unusually low-mass core within a dense CSM produced from its lost H layers. Such extensive mass-loss may require interaction with a binary companion, as inferred for other SNe IIb (e.g., Maund et al. 2004; Benvenuto et al. 2013; Prentice et al. 2020), or it may be more consistent with wave-driven outbursts caused by core neon burning in stars with $M_{\rm ZAMS} \approx 11\ M_\odot$ (Wu & Fuller 2021, 2022). Interaction between the SN ejecta and this CSM explains the blue colors and obscured ejecta features at early times, while the small ^{56}Ni mass and nebular spectrum indicate a low zero-age main-sequence mass. This interaction can lead to an overestimated progenitor radius—if the CSM was near enough to the progenitor, we may have observed the shock cooling of this extended CSM instead of the outer envelope of the progenitor. In the future, more detailed models and multiwavelength observations, in particular in the radio and X-rays, will be needed in order to infer SNe IIb progenitor mass-loss rates and CSM masses.

Given the weak H spectral features when compared to spectra of other SNe IIb, SN 2020bio may be an intermediary object between the Type IIb and Ib subclasses, representing a progenitor that was recently stripped almost entirely of its H-rich envelope. Transitional objects between SNe IIb and SNe Ib have been observed (Prentice & Mazzali 2017) and can be explained by different amounts of H remaining in the outer envelope at the time of explosion. More difficult to explain are the small ^{56}Ni and ejecta masses, which are lower than those measured for both SNe IIb and SNe Ib (e.g., Taddia et al. 2018). Some objects that exist in the literature with both low ejecta and ^{56}Ni masses and observed SCE are peculiar SNe Ib as well as Ca-rich transients. However, it is difficult to reconcile the photospheric-phase spectra of SN 2020bio, which are most similar to those of other SNe IIb, with the spectra of these objects, which are often used to argue for a degenerate or ultra-stripped progenitor (Yao et al. 2020; Jacobson-Galán et al. 2022). Instead, it is more likely that SN 2020bio had a massive star progenitor more similar to the progenitors of other SNe IIb based on their similar photospheric-phase spectral features.

Perhaps more interesting are the similarities between SN 2020bio and SN 2018gjx. SN 2018gjx is a peculiar object; Prentice et al. (2020) found that it showed evidence for CSM shock cooling at early times before displaying typical SN IIb spectra. Around 30 days after explosion, the spectra began showing strong emission features of He I that the authors argued were powered by interaction with He-rich material, revealed by the receding photosphere, that persisted into the nebular phase. Like SN 2020bio, it had a weak secondary light-curve peak that implied a synthesized ^{56}Ni mass of 0.021 $M_\odot$. A scenario that explains all these observations is an SN IIb explosion with an asymmetric ring or torus of CSM, viewed equatorially. The fact that the interaction signatures are not as prevalent in the spectra of SN 2020bio, both within the first few days of explosion and during the nebular phase, may suggest a viewing angle between equatorial and polar—if this is the case, more of the SN photospheric and nebular features would be visible, rather than obscured by the ongoing interaction. The CSM masses inferred from model fits for both objects are roughly the same ($\approx$0.01 $M_\odot$). This may reveal that the progenitor of SN 2020bio underwent extensive mass loss, perhaps losing almost all of its H-rich material before exploding. Even in this extreme case, however, the models used throughout this analysis (e.g., Piro 2015; Sapir & Waxman 2017; Piro et al. 2021) have been applied to both H-rich and H-poor objects. Therefore, we are confident our conclusions remain valid, regardless of the exact amount of H remaining in the progenitor envelope.

This study contributes to the overall diversity in the progenitors of SNe IIb. More systematic studies of SNe with observed SCE will be needed in order to search for similarities and differences in their progenitor systems. In particular, this work shows the importance of rapid, multiwavelength follow-up of these objects. It is particularly important to better understand the number of SNe IIb with weak secondary light-curve peaks, such as SN 2020bio. These objects may have later-time ($\geqslant$ 5 days) luminosity below the detection threshold of current all-sky surveys as well as rapid early-time emission that evolves too quickly to be extensively followed. Therefore, we may be undercounting the rates of core-collapse, stripped-envelope SNe with low ^{56}Ni and ejecta masses. A better understanding of their progenitors will be important for exploring the low-mass end of core-collapse SNe.

Acknowledgments

This work made use of data from the Las Cumbres Observatory network. The LCO group is supported by AST-1911151 and AST-1911225 and NASA Swift grant 80NSSC19k1639. I.A. is a CIFAR Azrieli Global Scholar in the Gravity and the Extreme Universe Program and acknowledges support from that program, from the European Research Council (ERC) under the European Union's Horizon 2020 research and innovation program (grant agreement No. 852097), from the Israel Science Foundation (grant No. 2752/19), from the United States—Israel Binational Science Foundation (BSF), and from the Israeli Council for Higher Education Alon Fellowship.

This work made use of the data products generated by the NYU SN group, and released under doi:10.5281/zenodo.58766, available at https://github.com/nyusngroup/SESNtemple/.

This work has made use of data from the Asteroid Terrestrial-impact Last Alert System (ATLAS) project. The Asteroid Terrestrial-impact Last Alert System (ATLAS) project is primarily funded to search for near-Earth asteroids through NASA grants NN12AR55G, 80NSSC18K0284, and 80NSSC18K1575; byproducts of the NEO search include images and catalogs from the survey area. This work was partially funded by Kepler/K2 grant J1944/80NSSC19K0112 and HST GO-15889, and STFC grants ST/T000198/1 and ST/S006109/1. The ATLAS science products have been made possible through the contributions of the University of Hawaii Institute for Astronomy, Queen's University Belfast, the Space Telescope Science Institute, the South African Astronomical Observatory, and The Millennium Institute of Astrophysics (MAS), Chile.

Software: `Astropy` (Astropy Collaboration et al. 2018), `emcee` (Foreman-Mackey et al. 2013), `lcogtsnpipe` (Valenti et al. 2016), Matplotlib (Hunter 2007), `MESA` (Paxton et al. 2011, 2013, 2015, 2018, 2019), Numpy (Harris et al. 2020), `STELLA` (Blinnikov et al. 1998, 2000, 2006).

Appendix
Corner Plots

In Figures A1, A2, A3, and A4, we present distributions of the fitted parameters of the models detailed in Section 4.2. In Figure A5, we present fits assuming a H-poor envelope composition, appropriate for a stripped-envelope SN, with best-fit parameter values given in Table A1.

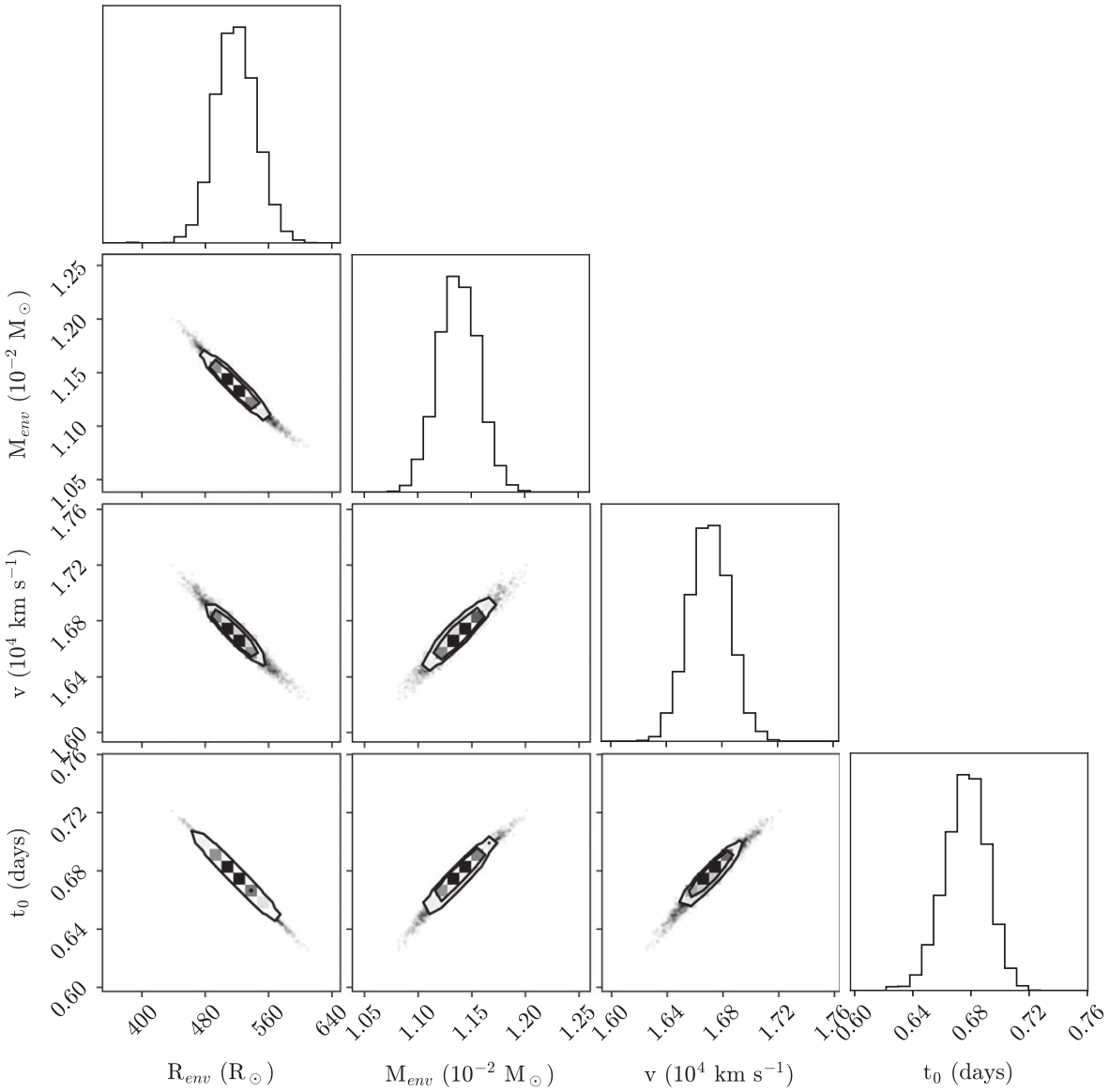

Figure A1. Corner plots showing the fitted parameter distributions for the P15 model.

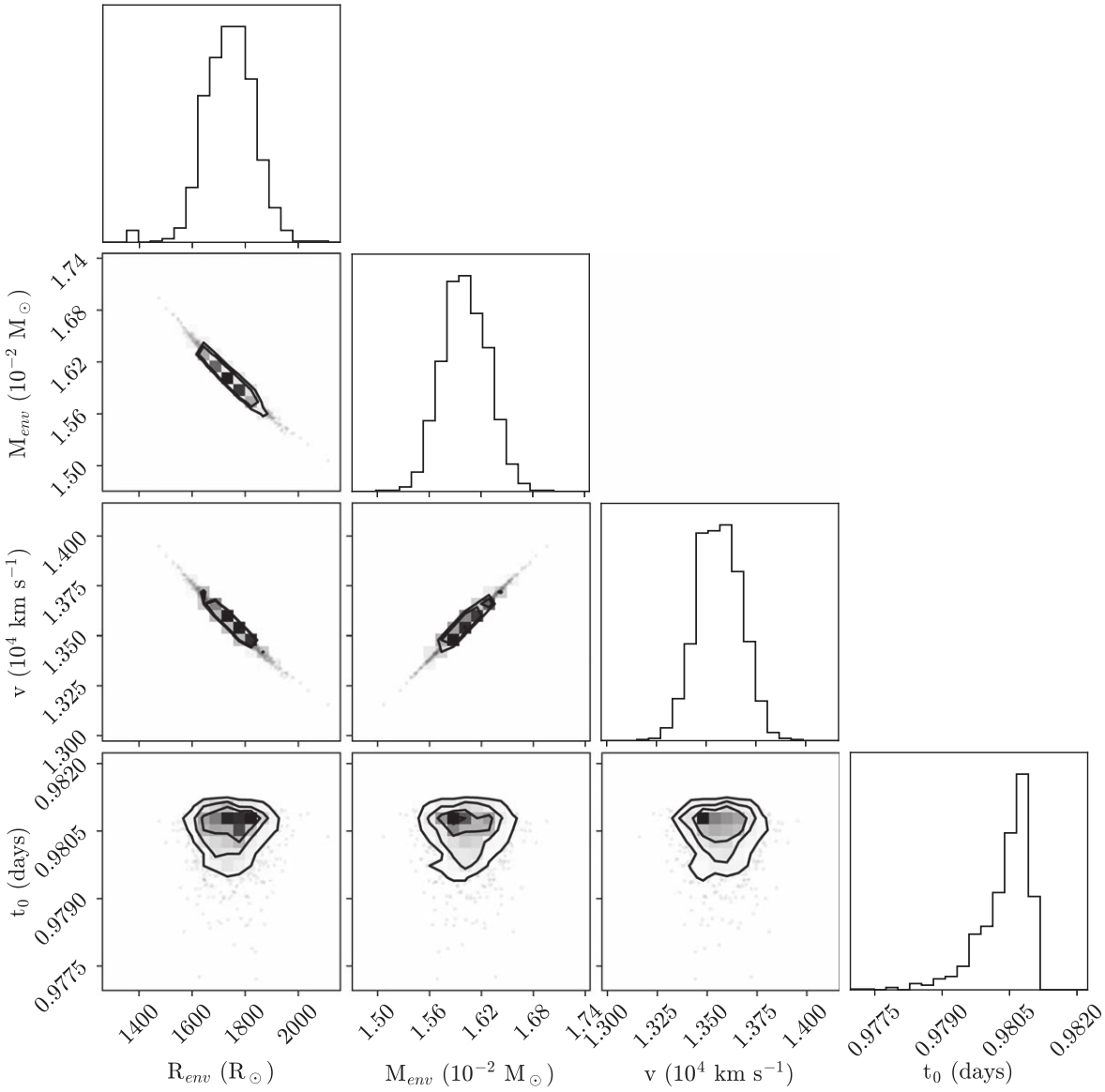

Figure A2. Same as Figure A1, but for the P21 model.

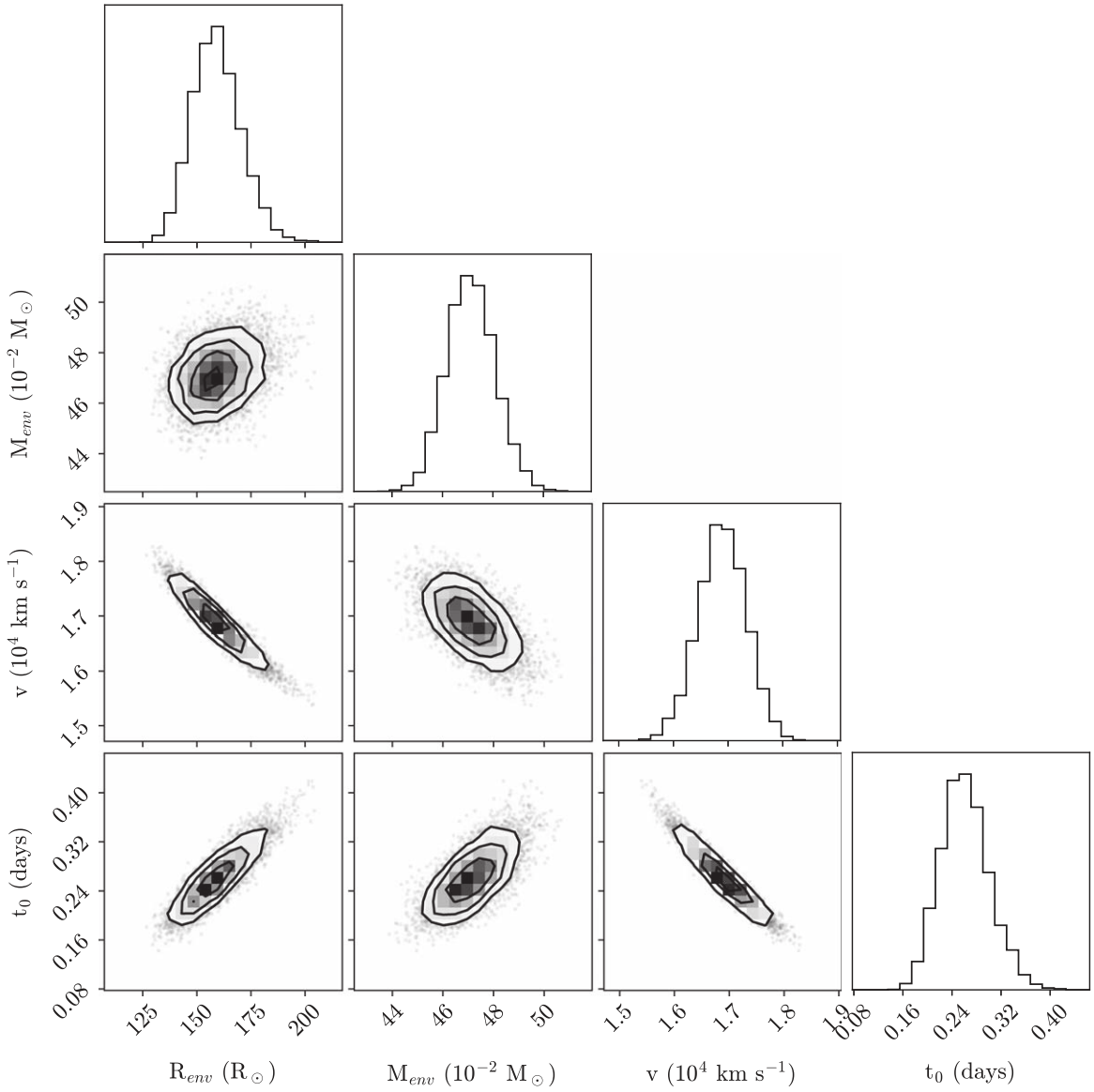

Figure A3. Same as Figure A1, but for the SW17 ($n = 3/2$) model.

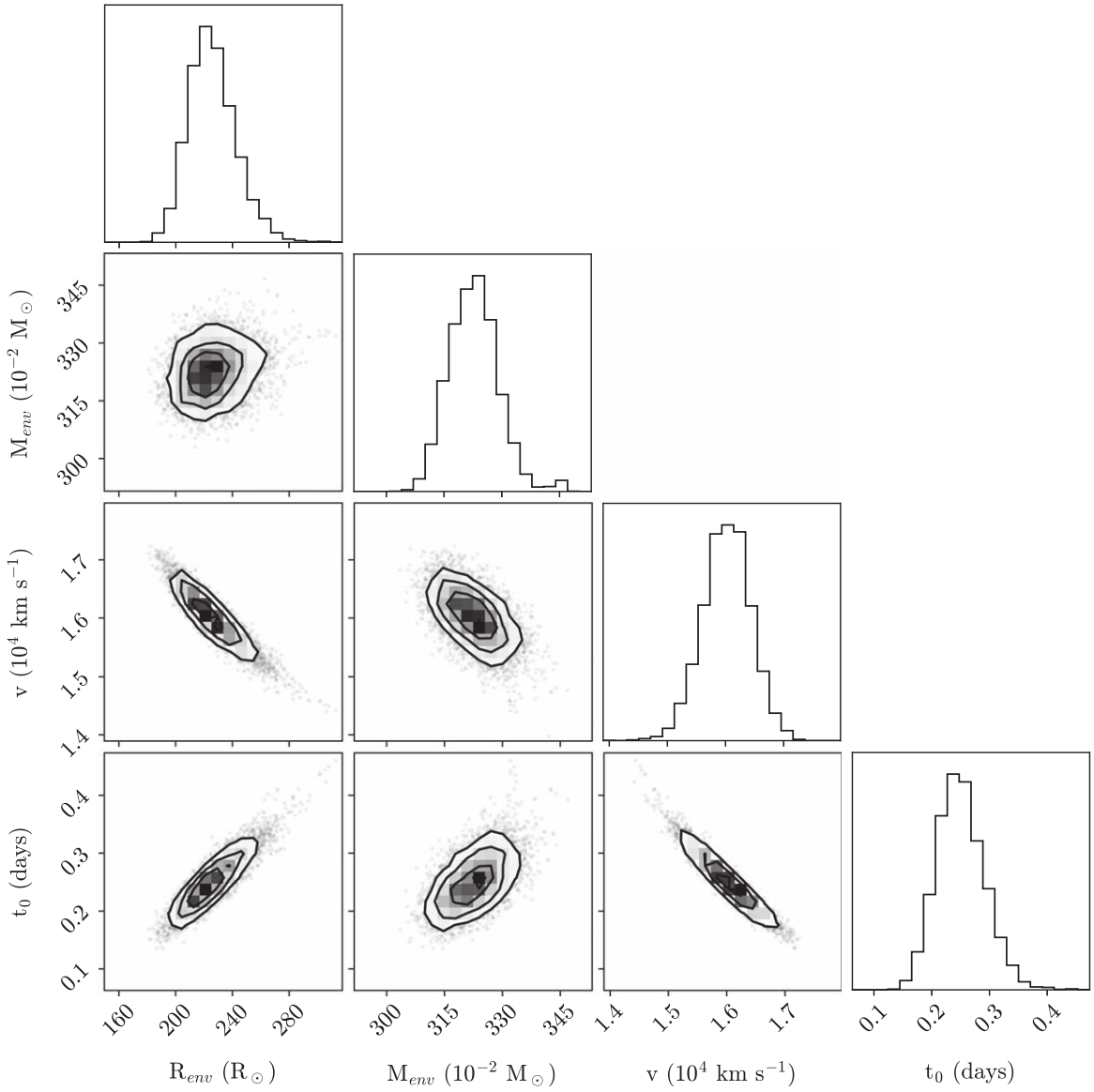

Figure A4. Same as Figure A1, but for the SW17 ($n = 3$) model.

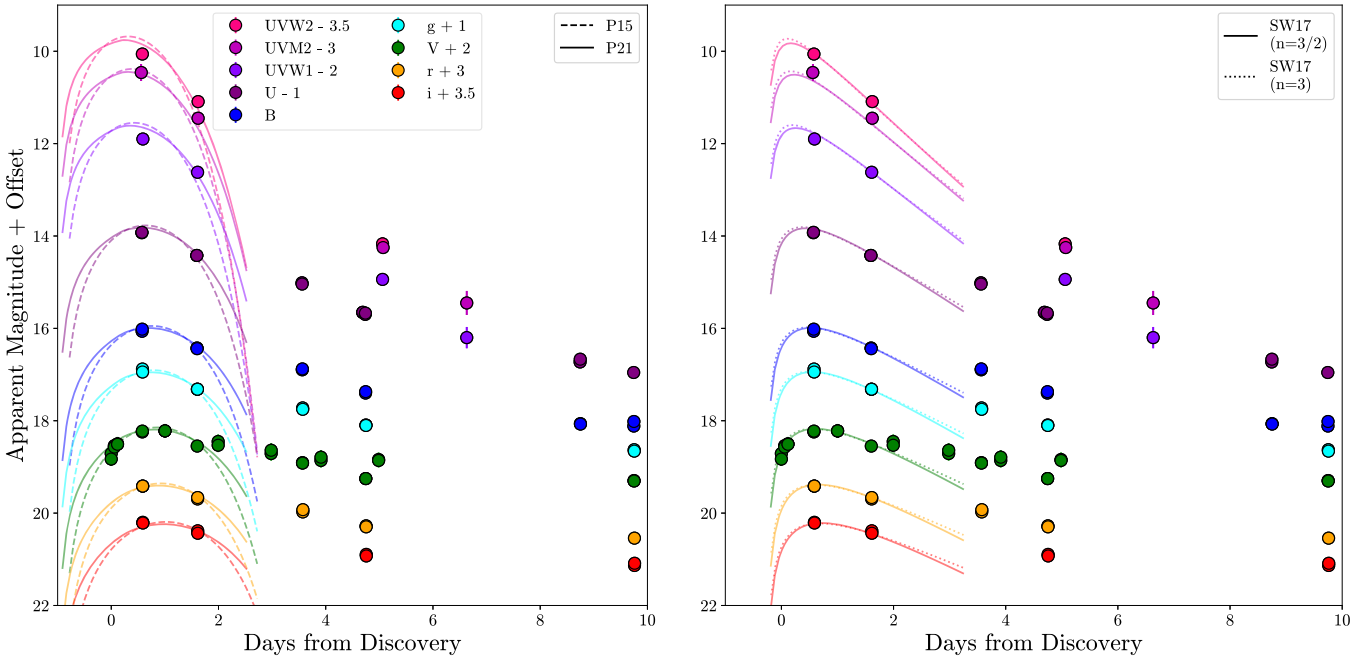

Figure A5. Same as Figure 7, but assuming a H-poor envelope composition ($\kappa = 0.20$ cm^2 g^{-1}). The fits are of comparable quality to those assuming a H-rich composition, but the best-fit parameters are quantitatively different (Table A1).

Table A1
SCE H-poor Model Parameters

Model	$R_{\rm env}$ ($R_\odot$)	$M_{\rm env}$ (10^{-2} $M_\odot$)	v^a (10^4 km s^{-1})	t_0 (days)	χ^2 / d.o.f.
P15	309^{+18}_{-17}	$1.94^{+0.03}_{-0.04}$	$1.67^{+0.02}_{-0.01}$	$0.78^{+0.01}_{-0.01}$	21.6
P21	1010^{+59}_{-81}	$2.74^{+0.07}_{-0.06}$	$1.36^{+0.02}_{-0.01}$	$0.98^{+0.01}_{-0.01}$	21.0
SW17 ($n = 3/2$)	$92^{+7.5}_{-8.4}$	$80.9^{+2.00}_{-1.70}$	$1.70^{+0.05}_{-0.06}$	$0.26^{+0.04}_{-0.04}$	8.7
SW17 ($n = 3$)	$140^{+11}_{-9.7}$	$857^{+16.6}_{-16.1}$	$2.50^{+0.07}_{-0.07}$	$0.25^{+0.05}_{-0.04}$	8.7

[a] **Note.** The characteristic velocity for P15 and P21 and the shock velocity for SW17.

ORCID iDs

C. Pellegrino https://orcid.org/0000-0002-7472-1279
D. Hiramatsu https://orcid.org/0000-0002-1125-9187
I. Arcavi https://orcid.org/0000-0001-7090-4898
D. A. Howell https://orcid.org/0000-0003-4253-656X
K. A. Bostroem https://orcid.org/0000-0002-4924-444X
P. J. Brown https://orcid.org/0000-0001-6272-5507
J. Burke https://orcid.org/0000-0003-0035-6659
N. Elias-Rosa https://orcid.org/0000-0002-1381-9125
C. McCully https://orcid.org/0000-0001-5807-7893
M. Modjaz https://orcid.org/0000-0001-7132-0333
E. Padilla Gonzalez https://orcid.org/0000-0003-0209-9246
T. A. Pritchard https://orcid.org/0000-0001-9227-8349

References

Aldering, G., Humphreys, R. M., & Richmond, M. 1994, AJ, 107, 662
Arcavi, I., Gal-Yam, A., Yaron, O., et al. 2011, ApJL, 742, L18
Arcavi, I., Hosseinzadeh, G., Brown, P. J., et al. 2017, ApJL, 837, L2
Armstrong, P., Tucker, B. E., Rest, A., et al. 2021, MNRAS, 507, 3125
Astropy Collaboration, Price-Whelan, A. M., Sipőcz, B. M., et al. 2018, AJ, 156, 123
Becker, A. 2015, HOTPANTS: High Order Transform of PSF ANd Template Subtraction, Astrophysics Source Code Library, ascl:1504.004
Benvenuto, O. G., Bersten, M. C., & Nomoto, K. 2013, ApJ, 762, 74
Blinnikov, S., Lundqvist, P., Bartunov, O., et al. 2000, ApJ, 532, 1132
Blinnikov, S. I., Eastman, R., Bartunov, O. S., et al. 1998, ApJ, 496, 454
Blinnikov, S. I., Röpke, F. K., Sorokina, E. I., et al. 2006, A&A, 453, 229
Blondin, S., & Tonry, J. L. 2007, ApJ, 666, 1024
Breeveld, A. A., Landsman, W., Holland, S. T., et al. 2011, in AIP Conf. Proc. 1358, Gamma Ray Bursts 2010, ed. J. E. McEnery, J. L. Racusin, & N. Gehrels (Melville, NY: AIP), 373
Brown, P. J., Breeveld, A. A., Holland, S., et al. 2014, Ap&SS, 354, 89
Bruch, R. J., Gal-Yam, A., Schulze, S., et al. 2021, ApJ, 912, 46
Ergon, M., Sollerman, J., Fraser, M., et al. 2014, A&A, 562, A17
Fang, Q., & Maeda, K. 2018, ApJ, 864, 47
Fang, Q., Maeda, K., Kuncarayakti, H., et al. 2019, NatAs, 3, 434
Fassia, A., Meikle, W. P. S., Chugai, N., et al. 2001, MNRAS, 325, 907
Filippenko, A. V. 1997, ARA&A, 35, 309
Filippenko, A. V., Matheson, T., & Ho, L. C. 1993, ApJL, 415, L103
Foreman-Mackey, D., Hogg, D. W., Lang, D., et al. 2013, PASP, 125, 306
Fransson, C., Lundqvist, P., & Chevalier, R. A. 1996, ApJ, 461, 993
Fremling, C., Ko, H., Dugas, A., et al. 2019, ApJL, 878, L5
Gal-Yam, A. 2017, in Handbook of Supernovae, ed. A. Alsabti & P. Murdin (Cham: Springer), 195
Gehrels, N., Chincarini, G., Giommi, P., et al. 2004, ApJ, 611, 1005
Harris, C. R., Millman, K. J., van der Walt, S. J., et al. 2020, Natur, 585, 357
Hiramatsu, D., Howell, D. A., Moriya, T. J., et al. 2021, ApJ, 913, 55
Howell, D. A., Sullivan, M., Perrett, K., et al. 2005, ApJ, 634, 1190
Hunter, J. D. 2007, CSE, 9, 90
Jacobson-Galán, W. V., Margutti, R., Kilpatrick, C. D., et al. 2020, ApJ, 898, 166
Jacobson-Galán, W. V., Venkatraman, P., Margutti, R., et al. 2022, ApJ, 932, 58
Janka, H.-T. 2012, ARNPS, 62, 407
Jerkstrand, A., Ergon, M., Smartt, S. J., et al. 2015, A&A, 573, A12
Landolt, A. U. 1992, AJ, 104, 340
Liu, Y.-Q., Modjaz, M., Bianco, F. B., et al. 2016, ApJ, 827, 90
Lyman, J. D., Bersier, D., James, P. A., et al. 2016, MNRAS, 457, 328
Maeda, K., Chandra, P., Moriya, T. J., et al. 2023, ApJ, 942, 17
Maeda, K., Hattori, T., Milisavljevic, D., et al. 2015, ApJ, 807, 35
Maund, J. R., Fraser, M., Ergon, M., et al. 2011, ApJL, 739, L37
Maund, J. R., Smartt, S. J., Kudritzki, R. P., et al. 2004, Natur, 427, 129
Modjaz, M., Li, W., Butler, N., et al. 2009, ApJ, 702, 226
Morales-Garoffolo, A., Elias-Rosa, N., Benetti, S., et al. 2014, MNRAS, 445, 1647
Morozova, V., Piro, A. L., & Valenti, S. 2018, ApJ, 858, 15
Nakaoka, T., Moriya, T. J., Tanaka, M., et al. 2019, ApJ, 875, 76
Nakar, E., & Piro, A. L. 2014, ApJ, 788, 193
Ofek, E. O., Sullivan, M., Shaviv, N. J., et al. 2014, ApJ, 789, 104
Paxton, B., Bildsten, L., Dotter, A., et al. 2011, ApJS, 192, 3

Paxton, B., Cantiello, M., Arras, P., et al. 2013, ApJS, 208, 4
Paxton, B., Marchant, P., Schwab, J., et al. 2015, ApJS, 220, 15
Paxton, B., Schwab, J., Bauer, E. B., et al. 2018, ApJS, 234, 34
Paxton, B., Smolec, R., Schwab, J., et al. 2019, ApJS, 243, 10
Piro, A. L. 2015, ApJL, 808, L51
Piro, A. L., Haynie, A., & Yao, Y. 2021, ApJ, 909, 209
Poznanski, D., Prochaska, J. X., & Bloom, J. S. 2012, MNRAS, 426, 1465
Prentice, S. J., Maguire, K., Boian, I., et al. 2020, MNRAS, 499, 1450
Prentice, S. J., & Mazzali, P. A. 2017, MNRAS, 469, 2672
Prentice, S. J., Mazzali, P. A., Pian, E., et al. 2016, MNRAS, 458, 2973
Pritchard, T. A., Roming, P. W. A., Brown, P. J., et al. 2014, ApJ, 787, 157
Rabinak, I., & Waxman, E. 2011, ApJ, 728, 63
Richmond, M. W., Treffers, R. R., Filippenko, A. V., et al. 1994, AJ, 107, 1022
Roming, P. W. A., Kennedy, T. E., Mason, K. O., et al. 2005, SSRv, 120, 95
Sapir, N., & Waxman, E. 2017, ApJ, 838, 130
Schlafly, E. F., & Finkbeiner, D. P. 2011, ApJ, 737, 103
Shingles, L., Smith, K. W., Young, D. R., et al. 2021, TNSAN, 7, 1
Shussman, T., Waldman, R., & Nakar, E. 2016, arXiv:1610.05323
Smith, J. A., Tucker, D. L., Kent, S., et al. 2002, AJ, 123, 2121
Smith, K. W., Smartt, S. J., Young, D. R., et al. 2020, PASP, 132, 085002
Smith, N. 2014, ARA&A, 52, 487
Smith, N., Li, W., Filippenko, A. V., et al. 2011, MNRAS, 412, 1522
Soderberg, A. M., Margutti, R., Zauderer, B. A., et al. 2012, ApJ, 752, 78
Springob, C. M., Haynes, M. P., Giovanelli, R., et al. 2005, ApJS, 160, 149
Srivastav, S., Smartt, S. J., McBrien, O., et al. 2020, TNSAN, 32, 1
Stetson, P. B. 1987, PASP, 99, 191
Strotjohann, N. L., Ofek, E. O., Gal-Yam, A., et al. 2021, ApJ, 907, 99
Taddia, F., Stritzinger, M. D., Bersten, M., et al. 2018, A&A, 609, A136
Tartaglia, L., Fraser, M., Sand, D. J., et al. 2017, ApJL, 836, L12
Terreran, G., Margutti, R., Bersier, D., et al. 2019, ApJ, 883, 147
Tonry, J. L., Denneau, L., Heinze, A. N., et al. 2018, PASP, 130, 064505
Tully, R. B., & Fisher, J. R. 1977, A&A, 54, 661
Valenti, S., Howell, D. A., Stritzinger, M. D., et al. 2016, MNRAS, 459, 3939
Van Dyk, S. D., Zheng, W., Fox, O. D., et al. 2014, AJ, 147, 37
Woosley, S. E., Eastman, R. G., Weaver, T. A., et al. 1994, ApJ, 429, 300
Woosley, S. E., & Heger, A. 2007, PhR, 442, 269
Wu, S., & Fuller, J. 2021, ApJ, 906, 3
Wu, S. C., & Fuller, J. 2022, ApJ, 930, 119
Yao, Y., De, K., Kasliwal, M. M., et al. 2020, ApJ, 900, 46
Yaron, O., & Gal-Yam, A. 2012, PASP, 124, 668
Yaron, O., Perley, D. A., Gal-Yam, A., et al. 2017, NatPh, 13, 510
Zacharias, N., Finch, C. T., Girard, T. M., et al. 2013, AJ, 145, 44